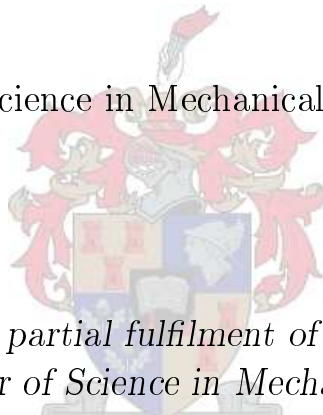# Performance of an Axial Flow Helium Compressor under High Through-Flow Conditions

by

## Christiaan Louis de Wet

Master of Science in Mechanical Engineering

*Thesis presented in partial fulfilment of the requirements for the degree of Master of Science in Mechanical Engineering at Stellenbosch University*

Department of Mechanical and Mechatronics Engineering,
University of Stellenbosch,
Private Bag X1, Matieland 7602, South Africa.

Supervisor:      Prof. T.W. von Backström
Co-supervisor:   Mr. S.J. van der Spuy

March 2010

# Declaration

By submitting this thesis electronically, I declare that the entirety of the work contained therein is my own, original work, that I am the owner of the copyright thereof (unless to the extent explicitly otherwise stated) and that I have not previously in its entirety or in part submitted it for obtaining any qualification.

Signature: ...........................

C.L. de Wet

Date: 16/02/2010 ..............................

# Abstract

## Performance of an Axial Flow Helium Compressor under High Through-Flow Conditions

C.L. de Wet

*Department of Mechanical and Mechatronics Engineering,*
*University of Stellenbosch,*
*Private Bag X1, Matieland 7602, South Africa.*

Thesis: MScEng (Mech)

March 2010

The purpose of this investigation is to determine the performance of an axial flow compressor operating in a closed loop helium cycle under high through-flow conditions. The GTHTR300 four-stage helium test compressor was chosen for this investigation. Limited information on the helium test compressor's blade profiles are available, therefore a mathematical model was developed to calculate the blade geometries based on the theory of Lieblein and Aungier. A locally available three-stage compressor was used to confirm whether the mathematical model calculated the blade profile geometries correctly. The Stellenbosch University Compressor Code (SUCC), an axisymmetric inviscid through-flow code, was used to compare the performance of the calculated three-stage compressor blade geometries with available experimental data. Excellent correlation was obtained, thus it was concluded that the mathematical model as well as the SUCC could be used to predict the performance of an axial flow compressor. The blade geometries of the helium test compressor were calculated and the pressure ratio and efficiency predictions of the SUCC correlated well with the experimental data. The helium test compressor was simulated to verify the calculated blade geometries further using the Computational Fluid Dynamics (CFD) package NUMECA FINE™/Turbo. The FINE™/Turbo pressure ratio and efficiency predictions compared adequately with the SUCC and available experimental data, especially in the design region. At high mass flow rates the stator blade row experiences negative incidence stall which results in a large recirculation zone in the stator blade wake.

# Uittreksel

## Eienskappe van 'n Aksiaalvloei Helium Kompressor Onderhewig aan Hoë Deurvloei Toestande

*("Performance of an Axial Flow Helium Compressor*
*under High Through-Flow Conditions")*

C.L. de Wet

*Departement Meganiese en Megatroniese Ingenieurswese,*
*Universiteit van Stellenbosch,*
*Privaatsak X1, Matieland 7602, Suid Afrika.*

Tesis: MScIng (Meg)

Maart 2010

Die doel van hierdie ondersoek is om vas te stel wat die werkverrigting is van 'n aksiale kompressor in 'n geslote lus helium siklus onderhewig aan hoë deurvloei kondisies. Die GTHTR300 vier-stadium helium toets kompressor is gekies vir die ondersoek. Daar is egter beperkte inligting oor die helium kompressor se lem geometrie, dus is 'n wiskundige model ontwikkel om dit te bereken gebaseer op die werk van Lieblein en Aungier. Om te bevestig dat die lem geometrie akkuraat was, was die lem geometrie van die 'n plaaslike beskikbare drie-stadium kompressor bereken. Die Stellenbosch University Compressor Code (SUCC), 'n aksisimmetriese nie-viskeuse deurvloei kode, is gebruik om die prestasie van die berekende lem geometrie met beskikbare eksperimentele data te vergelyk. Uitstekende korrelasie is verkry vir die drukverhouding en benuttingsgraad resultate, dus is die gevolgtrekking gemaak dat die wiskundige model sowel as die SUCC gebruik kon word om die lem geometrie en werkverrigting van aksiale kompressors te bereken en voorspel. Die helium toets kompressor is gesimuleer met behulp van die numeriese vloei-dinamika pakket NUMECA FINE™/Turbo om die berkende lem geometrie verder te verifieer. Die FINE™/Turbo drukverhouding en benuttingsgraad resultate het goed gekorreleer met beide die SUCC resultate en eksperimentele data, veral in die ontwerpsgebied. Teen hoë massa vloei tempo's vind daar groot wegbreking teen negatiewe invalshoek plaas in die stator lemry en dit veroorsaak 'n hersirkulasie sone in die naloop van die stator lem.

# Acknowledgements

I would like to thank my two supervisors, Professor T.W. von Backström and Mr S.J. van der Spuy for their constant guidance, support and advice. I would also like to thank Andrew Gill for his advice, encouragement and his assistance in understanding the 2-dimensional code and with axial flow compressors. I would like to give thanks to my brother, Andrew de Wet that helped me with the 3-dimensional code and input into numerical simulations.

# Dedications

*To my family and friends*

# Contents

# List of Figures

# List of Tables

# Nomenclature

**Variables**

| | | |
|---|---|---|
| $c$ | Blade profile chord length . . . . . . . . . . . . . . . | [ m ] |
| $h$ | Static enthalpy, blade height . . . . . . . . . . . . | [ kJ/kg, m ] |
| $i$ | Blade cascade incidence angle . . . . . . . . . . . . | [ deg ] |
| $\dot{m}$ | Mass flow rate . . . . . . . . . . . . . . . . . . . . | [ kg/s ] |
| $p$ | Pressure . . . . . . . . . . . . . . . . . . . . . . . | [ Pa ] |
| $r$ | Radial coordinate . . . . . . . . . . . . . . . . . . | [ m ] |
| $Re_{\mathrm{c}}$ | Blade chord Reynolds number . . . . . . . . . . . | [ ] |
| $s$ | Static entropy, blade pitch . . . . . . . . . . . . . | [ kJ/kg, m ] |
| $t_{\mathrm{b}}$ | Maximum blade profile thickness . . . . . . . . . . | [ m ] |
| $y^{+}$ | Dimensionless wall distance . . . . . . . . . . . . . | [ ] |
| $x$ | Axial coordinate . . . . . . . . . . . . . . . . . . . | [ m ] |
| $C$ | Absolute velocity . . . . . . . . . . . . . . . . . . | [ m/s ] |
| $DF$ | Diffusion factor . . . . . . . . . . . . . . . . . . . | [ ] |
| $D_{\mathrm{eq}}$ | Equivalent diffusion factor . . . . . . . . . . . . . | [ ] |
| $M$ | Mach number . . . . . . . . . . . . . . . . . . . . . | [ ] |
| $N_{\mathrm{row}}$ | Blade row number (sequential through the compressor) | [ ] |
| $R$ | Reaction ratio . . . . . . . . . . . . . . . . . . . . | [ ] |
| $T$ | Temperature . . . . . . . . . . . . . . . . . . . . . | [ K ] |
| $U$ | Blade velocity . . . . . . . . . . . . . . . . . . . . | [ m/s ] |
| $W$ | Relative velocity . . . . . . . . . . . . . . . . . . . | [ m/s ] |
| $Z$ | Number of blades in a blade row . . . . . . . . . . | [ ] |

**Greek letters**

| | | |
|---|---|---|
| $\alpha$ | Blade absolute leading or trailing edge flow angle . | [ deg ] |
| $\beta$ | Blade relative leading or trailing edge flow angle . | [ deg ] |
| $\delta$ | Deviation angle . . . . . . . . . . . . . . . . . . . . | [ deg ] |
| $\delta_{\mathrm{c}}$ | Blade tip clearance . . . . . . . . . . . . . . . . . . | [ m ] |
| $\gamma$ | Specific heat ratio . . . . . . . . . . . . . . . . . . | [ ] |

| | | |
|---|---|---|
| $\zeta$ | Stagger angle . . . . . . . . . . . . . . . . . . . . . . . . | [ deg ] |
| $\eta$ | Efficiency . . . . . . . . . . . . . . . . . . . . . . . . . | [ ] |
| $\theta$ | Camber angle . . . . . . . . . . . . . . . . . . . . . . . | [ deg ] |
| $\theta_w$ | Wake momentum thickness . . . . . . . . . . . . . | [ ] |
| $\kappa$ | Blade angle with the meridional direction . . . . . | [ deg ] |
| $\xi$ | Normalized incidence angle parameter . . . . . . . . | [ ] |
| $\rho$ | Density . . . . . . . . . . . . . . . . . . . . . . . . . . | [ kg/m$^3$ ] |
| $\phi$ | Flow coefficient . . . . . . . . . . . . . . . . . . . . | [ ] |
| $\psi$ | Load coefficient, Stream function . . . . . . . . . . . | [ ] |
| $\sigma$ | Blade row solidity . . . . . . . . . . . . . . . . . . . | [ ] |
| $\bar{\omega}$ | Total pressure loss coefficient . . . . . . . . . . . . . | [ ] |
| $\Delta$ | Difference . . . . . . . . . . . . . . . . . . . . . . . . | [ ] |

## Subscripts

| | |
|---|---|
| 0 | Total or stagnation thermodynamic conditions |
| 1 | Blade row inlet property |
| 2 | Blade row outlet property |
| $a$ | Axial |
| $c$ | Negative stall angle parameter or blade tip/seal clearence parameter |
| $des$ | Desired point |
| $eq$ | Equivalent |
| $ref$ | Reference point |
| $s$ | Positive stall angle parameter |
| $t$ | Total |
| $AOA$ | Angle of Attack |
| $\theta$ | Tangential component |
| $*$ | Sonic flow condition |

## Superscripts

| | |
|---|---|
| $*$ | Design condition |
| $'$ | Relative condition |

## Abbreviations

| | |
|---|---|
| AOA | Angle of Attack |
| CFD | Computational Fluid Dynamics |
| DNS | Direct Numerical Simulation |

EVO    Energieversorgung Oberhausen
HP     High Pressure
HPC    High Performance Computer
HHT    Hochtemperatur-Helium-Turbine
HHV    Hochtemperatur-Helium-Versuchsanlage
JAEA    Japan Atomic Energy Agency
JAERI   Japan Atomic Energy Research Institute
JNC    Japan Nuclear Cycle Development Institute
LP     Low Pressure
MHI    Mitsubishi Heavy Industries
MTFM   Matrix Through Flow Method
PBMR   Pebble Bed Modular Reactor
SCM    Streamline Curvature Method
SUCC   Stellenbosch University Compressor Code
GTHTR300  Gas Turbine High Temperature Reactor of 300 MWe

# Chapter 1

# Introduction

The purpose of this investigation is to determine the performance of an axial flow compressor operating in a closed loop helium cycle under high through-flow conditions. This chapter will serve as an introduction to the research by giving background information on the topic. A brief history on axial flow helium compressor research is presented, followed by the problem statement. The objectives for this study are then defined, followed by concluding remarks.

## 1.1 Background

This section will briefly cover the background of helium as a working fluid in axial flow compressors. It also describes the reason for this investigation. Previous closed loop axial flow helium compressor projects and their findings are also discussed.

### 1.1.1 General background

A Pebble Bed Modular Reactor (PBMR) is a first-of-its-kind 400 MWt (165 MWe) helium cooled nuclear reactor. The helium gas is heated by the nuclear fission process inside the reactor, and is used to generate electric energy by means of a closed cycle gas turbine power conversion unit. Therefore an axial compressor is required that can operate with helium as a working fluid.

Helium as working fluid has advantages and disadvantages in terms of compressor design and operation. A favourable aspect of helium is that the sonic speed is roughly three times that in air, due to helium having a lower molecular mass. Under Mach number scaling assumptions the ratio of the speed of rotation of a helium to an air compressor will be equal to the ratio of the sonic velocities, assuming that the two compressors operate at the same inlet stagnation temperature. A less favourable aspect is that helium is less compressible than air. This influences the design of helium axial flow compressors

to the extent that if the same pressure ratio is required, many more stages are needed to add energy to the helium. A larger number of stages means a longer flow passage that tends to impair the aerodynamic performance as a result of end-wall boundary layer growth and secondary flow. A longer rotor shaft also has an impact on the rotor dynamics (Takizuka *et al.*, 2004). Furthermore, the volume flow through the compressor is relatively small considering the unit's high power rating, as the compressor of a closed loop cycle is designed to operate at a much higher pressure level.

The safety of a power plant is important, especially in the case of a nuclear power plant such as the PBMR. Abnormal operating conditions may occur in a closed loop cycle that could influence the performance of the axial compressor, for instance the pressure vessel or a pipe can rupture. Under these off-design operating conditions, more flow than normal may be forced through the axial compressor. When this occurs, the axial velocity in the latter stages can increase and may lead to the blade rows operating outside the normal design envelope, and experiencing negative incidence stall. Under extreme conditions a negative pressure rise can occur across the axial compressor, however this is not part of the scope and will not be investigated.

### 1.1.2  Previous research

Weisbrodt (1995) presents a summary of the work done on high-temperature helium turbomachinery testing in Germany. Two experimental facilities were developed in Germany between 1968 and 1982 to investigate and develop closed-loop Brayton power cycles. The first was a cogeneration facility that supplied district heating and electricity that was managed by the municipal utility, Energieversorgung Oberhausen (EVO). The second experimental facility was the High Temperature Helium Test Plant (HHV) that was used to develop helium turbomachinery and components.

The EVO test plant had a design electrical power output of 50MW and a heating power output of 53.5MW (district heat). It consisted of a low pressure (LP) and high pressure (HP) compressor. The former had an inlet temperature and pressure of 25°C and 1.05 MPa, respectively. The latter had the same inlet temperature, but with an inlet pressure of 1.54 MPa. The rotor shaft of the LP compressor was coupled using a gearbox to the common rotor shaft of the HP compressors and HP turbine that rotated at 5500 rpm so that the rotor shaft of the LP compressor rotated at 3000 rpm. The LP compressor consisted of ten stages and the blades were designed with a reaction ratio of 100%. The HP compressor consisted of 15 stages and the same procedure was used to design the blades with the same reaction ratio as the LP compressor.

The turbomachinery of the EVO test facility operated for 24 000 hours. Since helium compressors have relatively long shafts, they are prone to vibration problems that can lead to bearing damage. During the operation of this facility it encountered vibration problems due to the long shafts. To reduce this effect the first critical frequency was made as high as possible and shaft seals with turbulence straightening sheets were used. These sheets are used to straighten the flow in shaft seals and reduce the turbulence. In addition to this the compressor used tilting segment bearings where it was possible.

A maximum electrical power output of only 28 MW could be achieved due to seal problems, bearing problems and thermal distortions. These problems were rectified and afterwards the plant achieved an electrical power of 30.7 MW. It could not achieve the nominal capacity of 50 MW was due to the turbomachinery components. The blade efficiency was low and the mass flow rate of the helium used for the cooling and sealing gas was more than the design value. Also that the inlet passage did not align the flow correctly for the first blade row.

Due to financial problems the turbomachinery components were not altered to reduce the power deficit, but the following suggestions were given. (1) The flow conditions of the inflow and outflow areas could be optimized in order to obtain the required flow onto the blades. (2) The blade gap losses had to be reduced by reducing the vibrations and using better suited materials so that the thermal expansion of blades could be at an optimum to achieve the desired tip clearance at operating conditions.

A new concept for the turbomachinery components was developed. It was decided that a reaction ratio of 50% would be better suited but this in turn increased the required number of blade rows. The turbomachinery ran at 90 Hz requiring a gear box between the turbomachinery components and generator.

As stated previously the HHV facility was used to develop a high-temperature reactor with a direct-cycle, helium turbine of large capacity (HHT). A fossil fuel fired heater was used by the facility instead of a nuclear heat source. Peak temperature of the test facility was around 850°C and up to 1000°C for shorter periods. The test circuit resembled a closed-loop gas turbine plant with a design pressure of 5 MPa and flow rate of 212 kg/s and the compressor needed 90 MW to drive it. A synchronous-motor was used to drive the compressor at 3000 rpm. The compressor had eight stages with 56 rotor blades and 72 stator blades.

When the HHV facility was commissioned, it encountered several problems. Firstly the seals of the turbomachinery leaked, due to ineffective human man-

agement and to mechanical defects. The flange joint on the main circuit leaked helium and was rectified by welding it shut. Small local gaps also appeared due to non-uniform temperature distributions. To prevent this, the temperature distributions were optimized by distributing the cooling gas more effectively and altering the flow rate.

The HHV facility operated for 325 hours at the design temperature of 850°C. It was shut down due to the termination of the high temperature helium turbine (HHT) project in Germany by the German government.

## 1.2    Problem statement

A reference helium compressor was required for the investigation, but data for a closed loop system as in the case of a PBMR is limited. Some of the specific design details of the PBMR compressor are not publicly available, due to contractual agreements between PBMR Ltd. and Mitsubishi Heavy Industries (MHI), which has the design, development, and manufacturing responsibilities for the gas turbine turbomachinery. Therefore a helium compressor test case had to be obtained with reasonable information to investigate it. The case study should also contain experimental data so that the results can be compared.

In 2004 the Japan Atomic Energy Research Institute (JAERI) carried out a design and developmental project called the gas turbine high temperature reactor with 300 MWe nominal-capacity (GTHTR300). A prototype helium compressor and a one-third scale test model of the prototype were designed. The test model consists of four stages and a helium gas loop was designed and fabricated (Yan *et al.*, 2003; Takizuka *et al.*, 2004; Yan *et al.*, 2008) to obtain the experimental results of the test model. The four stages were geometrically similar to that of the GTHTR300 prototype compressor. All the specifications of the compressor were given, except for the blade profile geometry. The test model compressor was used as a basis for the investigation.

The helium test compressor had to be investigated and the key issues related to the performance of a helium axial compressor under high through-flow conditions must be quantified. In order to predict the performance, the blade profile geometry of the helium test compressor had to be reverse engineered and the results compared to the experimental data available in Yan *et al.* (2008). Thus a mathematical model had to be compiled and verified; therefore the Rofanco three-stage compressor was used as a test case by comparing the pressure ratio performance predictions of the calculated and exact blade profile geometries.

## 1.3   Objectives of this thesis

The main objective of this thesis is:

- To investigate and evaluate the performance of a helium compressor under high through-flow conditions and compare the performance predictions to available experimental data for the helium compressor.

The secondary objectives are:

- To compile a mathematical model that must produce reasonably adequate blade profile geometries for a compressor with available design specifications.

- To verify the mathematical model with test cases and obtain sufficient results using the 2-dimensional Stellenbosch University Compressor Code (SUCC) and the 3-dimensional Computational Fluid Dynamics (CFD) package NUMECA FINE™/Turbo.

- To investigate the blade rows at high through-flow conditions to identify if negative incidence stall occurs.

## 1.4   Concluding remarks

This thesis was required to investigate a helium compressor in a closed-loop cycle. The blade profile geometry of the helium compressor that was chosen for the investigation was not available, therefore a mathematical model was developed to calculate the blade profile geometry with the design specifications known. It was necessary to become familiar with the design and operation of axial flow compressors, thus Chapter 2 contains the description and discussion of these topics. Chapter 3 describes the theory and assumptions used in the mathematical model and then the compressor models for the test cases are given. Chapter 4 and Chapter 5 explain, and discuss how the 2-dimensional and 3-dimensional simulations were performed with respect to computational grids and boundary conditions. The results are provided and useful conclusions are drawn from them with a summary of the results at the end of each chapter. Chapter 6 is a summary of the investigation and subjects that require further research are mentioned.

# Chapter 2

# Axial flow compressor theory

In this chapter the need to understand an axial compressor stage will be covered by looking at the velocity triangles and a blade cascade. The terminology and theory of turbomachinery will be briefly covered. The loss models in a compressor stage are then investigated. An explanation of stall and other phenomena within turbomachinery, including negative incidence stall are given. At the end of this chapter there is a brief section on the four-quadrant map of an axial compressor.

## 2.1 Compressor stage

This section will cover the expressions and theory needed to understand an axial compressor stage. Firstly by defining the velocity triangles and then the blade cascade.

### 2.1.1 Velocity triangles

Velocity triangles are used to relate the flow properties and geometrical specifications of an axial compressor stage. This diagram is a very useful concept for axial compressor design and is therefore of importance in this investigation. The vector size and direction indicate the velocities entering and leaving a blade row. The velocities entering the blade row are labelled the leading edge velocities and the velocities leaving are the trailing edge velocities. This section discusses these velocity vectors. Refer to figure 2.1 for the velocity triangles. The figure is a cross section of a axial compressor stage and viewed towards the axis.

The subscripts 1 and 2 designate the inlet and exit of a blade row, respectively. The flow enters the blade row with a velocity, $W_1$, and at an angle, $\beta_1$, measured from the axial direction. The same definition is valid for the flow leaving the blade row at a velocity and flow angle, but with respect to the exit,
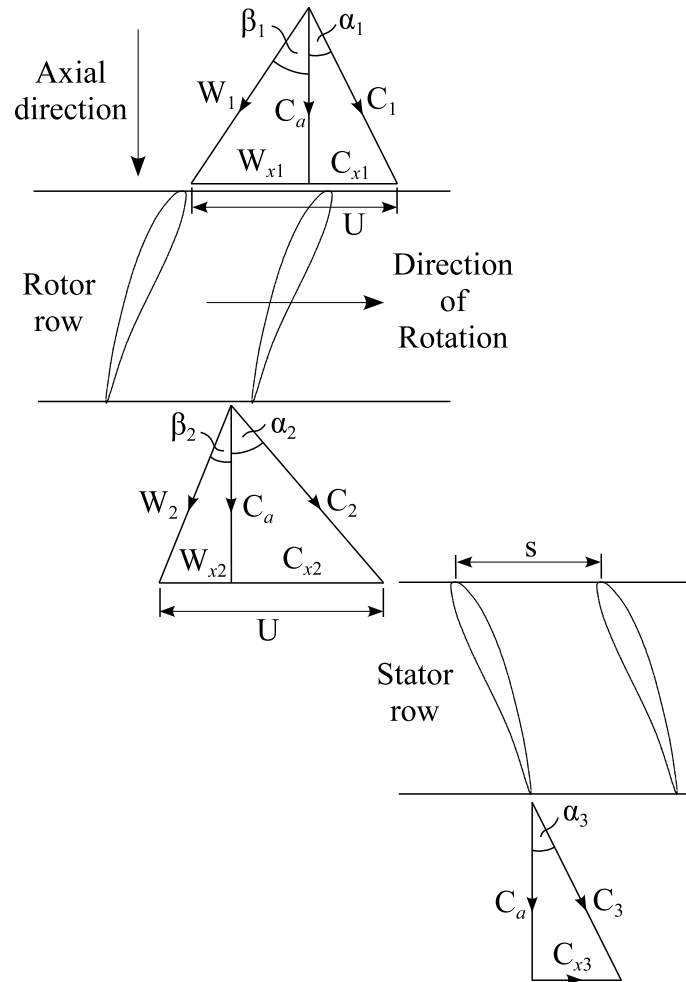
Figure 2.1: Velocity triangles for an axial flow compressor stage

therefore $W_2$ and $\beta_2$, respectively. $W$ and $\beta$ are termed the *relative velocity* and *relative flow angle*, respectively. The *blade velocity*, $U$, is the tangential velocity at which the blades are rotating. The flow that exits the previous blade row enters the following blade row at an angle, $\alpha_1$, with a velocity, $C_1$. The same description as mentioned previously for the relative velocity leaving the blade row, applies here, thus the velocity exits with an angle, $\alpha_2$ and velocity $C_2$. $C$ and $\alpha$ are termed the *absolute velocity* and *absolute flow angle*, respectively.

The subscript 3 refers to the exit of the stator blade. If two consecutive stages are similar in geometry, it is said to be normal, therefore $C_1 = C_3$ and $\alpha_1 = \alpha_3$. The relative velocity is the vector difference between the absolute and blade velocities. The relative velocity behind the rotor blade is less than in front of it. This shows that diffusion has taken place with a static pressure rise across the blade. The flow direction of the working fluid is changed towards

the axial direction due to the camber in the blade, therefore the flow area is increased with respect to the inlet, thus causing diffusion to take place. Diffusion also takes place in the stator blade row, where the absolute velocity turns towards the axial direction, thus ensuring a further static pressure rise. The stator blades also induce a static pressure rise on the working fluid, but this is considerably less than that of the rotor blades in an axial compressor with a high reaction ratio as is the case in this investigation.

## 2.1.2   Blade cascades

The flow between blades in a blade row of an axial flow compressor is often modelled as a two dimensional plane, this method is termed a *blade cascade*. This section describes the blade cascade nomenclature and how it is modelled. For a graphical explanation of the blade cascade nomenclature, see figure 2.2 that is similar to a figure found in Aungier (2003).
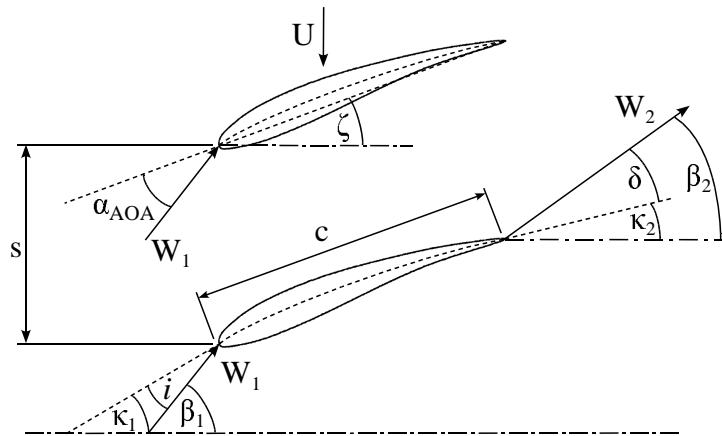


Figure 2.2: Blade cascade nomenclature

The *mean camberline* is a line running through the origins of the circles inscribing the blade profile. The *chord line*, $c$, of a blade is defined as a straight line between the leading and the trailing edge. The pitch, $s$, is the gap between neighbouring blades measured tangentially between their camber lines.

The angles between the axial direction and the camberline are defined as the *blade angles*, $\kappa_1$ and $\kappa_2$. The blade angle is the angle at which the flow will enter and leave the blade if it is run at the design conditions and there were no interferences to the flow path. The *incidence angle*, $i$, can be determined by equation (2.1.1) and is defined as the angle between the leading edge flow angle, $\beta_1$, and the blade angle, $\kappa_1$. The *deviation angle*, $\delta$, can be calculated by equation (2.1.2) and has the same definition as the incidence angle, but it

is with respect to the trailing edge, thus the angle between $\beta_2$ and $\kappa_2$. The *camber angle*, $\theta$, is the difference between the leading and trailing edge blade angles, $\kappa_1$ and $\kappa_2$ and can be calculated by equation (2.1.3). The *stagger angle*, $\zeta$, is the angle between the relative flow angle and angle of attack and can be determined by equation (2.1.4). It is convention to define the stagger angle as $\gamma$ like in Aungier (2003), but this is the same symbol used to indicate the specific heat ratio of a fluid, thus $\zeta$ is used here to avoid confusion. Cumpsty (1989) uses $\xi$ to indicate the stagger angle, but this is the same symbol used by Aungier (2003) to indicate the normalized incidence angle parameter which will be explained later on in this chapter. For a standalone blade that is not arranged in a cascade, the *angle of attack*, $\alpha_{AOA}$, is the angle between the inlet velocity vector and the chord line, according to Aungier (2003). This is the same as the angle between the inlet relative flow angle and stagger angle, as both these angles are with respect to the axial direction.

$$i = \beta_1 - \kappa_1 \qquad (2.1.1)$$

$$\delta = \beta_2 - \kappa_2 \qquad (2.1.2)$$

$$\theta = \kappa_1 - \kappa_2 \qquad (2.1.3)$$

$$\zeta = \beta_1 - \alpha_{AOA} \qquad (2.1.4)$$

## 2.2   Turbomachinery terminology and theory

Turbomachinery is a vast field and includes many types of machines that have been widely researched. The axial compressor will be the focus here and some general information necessary to understand the abbreviations used in this document will be covered. However, the emphasis will not be to provide detailed explanations. The reader may consult Aungier (2003), Cumpsty (1989) and Dixon (1998) for further information on this subject.

The degree of reaction or reaction ratio, $R$, is an important quantity which is defined in Cumpsty (1989) and can be seen in equation (2.2.1). This factor indicates the fraction of the stage static enthalpy rise occurring in the rotor, disregarding losses.

$$R = \frac{\Delta h_{rotor}}{\Delta h_{stage}} = \frac{W_1^2 - W_2^2}{2U\left(W_{\theta 1} - W_{\theta 2}\right)} \qquad (2.2.1)$$

$W_1$ and $W_2$ are the leading and trailing flow velocities relative to the rotor blades, whereas $W_{\theta 1}$ and $W_{\theta 2}$ are the tangential components. According to Dixon (1998) the optimum reaction ratio is $R = 0.5$, where the pressure rise across a stator and rotor is the same. However in the GTHTR300 4-stage helium test compressor, the reaction ratio is significantly higher.

Dixon (1998) presents definitions for the total-to-total pressure coefficient, $\bar{\omega}$, flow coefficient, $\phi$, and stage load coefficient, $\psi$, which can be seen in equation (2.2.2), (2.2.3) and (2.2.4), respectively.

$$\bar{\omega} = \frac{\Delta p_0}{\frac{1}{2}\rho U^2} \tag{2.2.2}$$

$$\phi = \frac{C_a}{U} \tag{2.2.3}$$

$$\psi = \frac{\Delta h_0}{U^2} \tag{2.2.4}$$

The total-to-total pressure coefficient is the total pressure difference divided by the dynamic pressure based on the blade tip speed. The flow coefficient is the ratio between the axial velocity component and the blade speed. The stage load coefficient is the total enthalpy change across a stage over the blade speed. These coefficients are a function of the blade tangential velocity which changes with respect to blade height position.

Low pressure (suction side)



High pressure (pressure side)
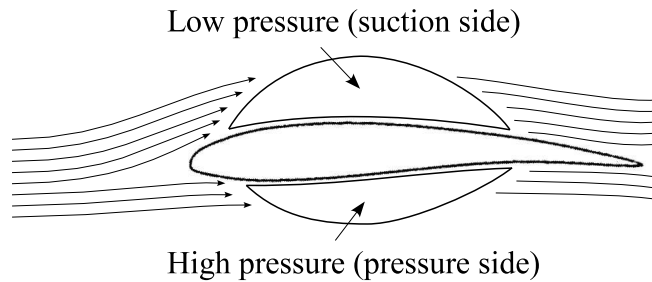
Figure 2.3: Fluid flow around a blade

The diffusion factor, $DF$, derived by Lieblein *et al.* (1953) is a measure of blade loading or an indication of the loading limit. This factor is essentially the ratio of the difference between the maximum velocity on the suction side of a blade and trailing edge velocity to the leading edge velocity. Refer to equation (2.2.5) for an expression of the diffusion factor as it is given in Aungier (2003). Figure 2.3 shows the distinction between the pressure and suction side of a blade. The $DF$ is used extensively in stall prediction models and is an indication of the thickness of the boundary layer near the blade surface and it is also an indication whether separation will occur on the suction side of the blade. If separation does occur, the blade profile losses will increase and this will be an indication that stall has occurred.

$$DF = \frac{1}{W_1}\left(W_1 - W_2 + \frac{\Delta W_\theta}{2\sigma}\right) \approx \frac{W_{max} - W_2}{W_1} \tag{2.2.5}$$

The equivalent diffusion factor, $D_{eq}$, was derived by Lieblein (1959) from experimental cascade data for NACA 65-series and C4 circular-arc blades. It can

be approximated as the ratio of the maximum velocity on the suction side of a blade to the trailing edge velocity as can be seen in equation (2.2.6).

$$D_{eq} \approx \frac{W_{max}}{W_2} \qquad (2.2.6)$$

Lieblein (1959) developed an equivalent diffusion factor correlation based upon blades operating at minimum loss, thus at the design incidence angle. This factor is defined in equation (2.2.7), as stated in Aungier (2003).

$$D_{eq}^* = \frac{\cos \beta_2^*}{\cos \beta_1^*} \left[ 1.12 + 0.61 \frac{\cos^2 \beta_1^*}{\sigma} \left( \tan \beta_1^* - \tan \beta_2^* \right) \right] \qquad (2.2.7)$$

To permit use of the equivalent diffusion factor as an off-design diffusion limit, Lieblein (1959) extended equation (2.2.7) to include operation at incidence angles greater than the design incidence angle. The off-design equivalent diffusion factor for $i \geq i^*$ can be calculated by equation (2.2.8), as stated in Aungier (2003). In equation (2.2.8) the $\Delta i^*$ term represents the difference between the incidence angle and reference incidence angle at minimum loss. The reference incidence angle will be explained later in Section 2.4.2. The parameter, $a$, is a representation for different blade profiles, being 0.0117 for the NACA 65-series blades and 0.007 for the C4 profile on a circular arc camber line. Cumpsty (1989) also defines the equivalent diffusion factor. It is similar to the formulation given by Aungier, except that it is with respect to the blade angles, $\kappa_1$ and $\kappa_2$ instead of the flow angles, $\beta_1$ and $\beta_2$.

$$D_{eq} = \frac{\cos \beta_2}{\cos \beta_1} \left[ 1.12 + a \left( \Delta i^* \right)^{1.43} + 0.61 \frac{\cos^2 \beta_1}{\sigma} \left( \tan \beta_1 - \tan \beta_2 \right) \right] \qquad (2.2.8)$$

## 2.3 Loss modelling

This section describes a method on how to calculate the losses in a blade cascade and specifically the blade tip clearance loss model. In Aungier (2003) a method is described of calculating the losses in a compressor blade cascade. Firstly the design angle of attack, $\alpha^*$, design incidence, $i^*$, and design deviation, $\delta^*$, angles have to be determined. These parameters are dependent on the camber angle, thus by implementing an iterative process these parameters can be obtained. Correlations are given in Aungier (2003) by fitting curves to the data of Johnsen and Bullock (1965). These correlation were developed by Lieblein (1960) which is also accessible in Johnsen and Bullock (1965). The next parameter needed is the design equivalent diffusion factor, $D_{eq}$, of Lieblein (1959). Succeeding this, Aungier (2003) gives a method of calculating the design total pressure loss coefficient at the design incidence angle derived by Lieblein (1959).

This loss coefficient only accounts for profile losses. To obtain a better and more realistic loss coefficient, additional loss models must be added to account for other losses. Aungier (2003) describes some of the losses: Mach-number effects, shock wave loss for supersonic cascades, blade tip clearance and shroud seal leakage loss. The method that Aungier (2003) uses is built on the work of Howell (1945). The losses are then altered to account for off-design conditions. When all the losses have been obtained, they can be added to form a single loss coefficient. By adding the loss coefficients, the correct pressure difference across a blade row can be calculated.

To account for off-design performance, Aungier (2003) developed a model with the approximations of Lieblein (1959). What follows is an overview of this model. Refer to Appendix B for a detailed description of this model. Firstly, the range that the incidence angle deviates from the design incidence angle is calculated. This range is then used to determine the minimum loss incidence angle and then the minimum loss coefficient, $\bar{\omega}_m$. A normalized incidence angle parameter, $\xi$, is defined and used to calculate the off-design loss coefficient, $\bar{\omega}$. A simple parabola near the design region represents the loss coefficient and linear extrapolations from the parabola represent the loss coefficient far from the design point. Figure 2.4 shows the parabolic loss bucket used to calculate the off-design loss coefficient with the linear extrapolations indicated.
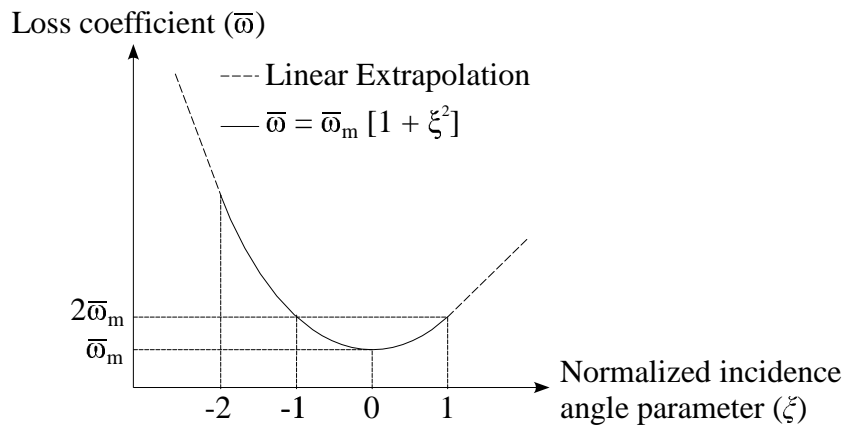


Figure 2.4: Off-design loss bucket

The model described above and discussed in Appendix B is implemented in the Aungier module of the SUCC. It was coded by Thiart (2004) and refined by Gill (2006). What follows in the next section is a more detailed description of the blade tip clearance loss model. This loss model was not originally coded into the SUCC, therefore the theory is given in the next section as background. For the models incorporated into the SUCC, refer to Section 4.1.

## 2.3.1 Blade tip clearance loss

Aungier (2003) presents a model describing the tip and hub clearance or leakage losses. What follows is a description of this loss model and how to implement it in a through-flow code.

Rotor blades have a clearance near the casing and a fraction of the flow passes through this gap. The flow through the gap dissipates energy and thus it represents a loss in the system. Aungier calculates the total pressure difference between the pressure and suction side of the blade to quantify the clearance gap pressure leakage loss. See figure 2.5 for the tip clearance geometry of a rotor blade.
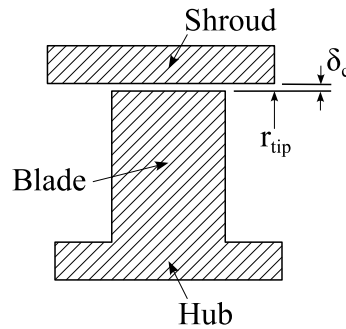


Figure 2.5: Blade tip clearance geometry

Aungier states that the pressure difference across the blade itself must balance the torque as given in equation (2.3.1).

$$\tau = \pi \delta_c \left[ (r\rho C_m)_1 + (r\rho C_m)_2 \right] \left[ r_2 C_{\theta 2} - r_1 C_{\theta 1} \right] \tag{2.3.1}$$

By using the torque the average pressure difference across the blade in the blade row can be calculated in equation (2.3.2), where $Z$ is the number of blades in a blade row.

$$\Delta p = \frac{\tau}{Z r_{tip} \delta_c c \cos \zeta} \tag{2.3.2}$$

The fluid velocity through the clearance gap, see equation (2.3.3), is estimated using the pressure difference given in equation (2.3.2). Equation (2.3.3) makes use of the assumed throttling coefficient of Aungier (2000). This coefficient is for the first blade row and reduces as the blade row number increases.

$$U_c = \frac{0.816}{N_{row}^{0.2}} \sqrt{\frac{2\Delta p}{\bar{\rho}}} \tag{2.3.3}$$

The clearance gap mass flow rate can be calculated by using equation (2.3.4).

$$\dot{m}_c = \bar{\rho} U_c Z \delta_c c \cos \zeta \tag{2.3.4}$$

The clearance gap total pressure loss can be calculated by using the pressure difference across the blade and mass flow rate of the clearance gap as can be seen in equation (2.3.5).

$$\Delta p_{t,c} = \Delta p \frac{\dot{m}_c}{\dot{m}} \tag{2.3.5}$$

The clearance gap is located near the casing which is in the end-wall region. This loss will accumulate together with the end-wall boundary layer losses for each blade row, resulting in the through-flow analysis to diverge due to the pressure losses at the tip exceeding the pressure rise. Secondary flows in a compressor blade row cause the flow to be mixed, but a conventional through-flow analysis does not account for this. Therefore a loss stays along a stream sheet throughout the compressor. To ensure that divergence does not occur, Aungier imposes the clearance gap total pressure as a linear distribution along the annulus. When this linear distribution is integrated the value must equal the result given in equation (2.3.5), but with a zero pressure loss at the wall opposite from the clearance gap.

When a compressor consists of stator blades that contain a seal clearance, the same model described above by Aungier can be used, with the exception that the clearance gap is located at the hub.

## 2.4    Description of compressor phenomena

Several phenomena occur in axial flow compressors, namely stall, surge and choke. There are others, but these are the most prominent. There is usually confusion between stall and surge, but these are two completely different types of phenomena. Stall occurs before surge, thus the conditions that induces stall is usually predicted. Stall is less damaging on the compressor blade rows, therefore a compressor can operate with some stall or with tiny stall cells stirring in some of the blade rows. If surge takes place, the efficiency drops dramatically and there is almost no pressure difference across the compressor. What follows is an explanation of these phenomena, obtained from Cumpsty (1989) and Pampreen (1993). Another type of phenomenon that occurs is negative incidence stall, this is also discussed as it is stated in Aungier (2003).

### 2.4.1    Stall, surge and choke

When stall is induced in an axial flow compressor the passages inside the rotor or stator row is partly blocked by one or several parts of the working fluid recirculating due to the flow separating from the blade. This part of the working

fluid is known as a stall cell. When stall occurs inside a compressor, there will be a large drop in outlet pressure. However the compressor can still operate, although the performance is very poor. As mentioned the blade or blade row can stall, but this does not mean that the compressor has stalled. Once sufficient stalling has occurred of several blades or blade rows, the compressor can not sustain a positive pressure rise and thus the compressor starts to experience surge. Surge will be explained later in this section.

Cumpsty (1989) and Pampreen (1993) gives an explanation on how a stall cell is formed and how it propagates inside an axial compressor. When a compressor blade is stalled, the angle of the flow striking the blade is relatively large and this causes the flow to separate much earlier. The separation can be the result of inaccurate alignment of the blades. Separation happens to more than one blade and a stall cell is formed. Afterwards the separation of flow increases and causes the passage between the blades to be blocked. Once one passage is blocked, it affects the adjacent passage. The incidence angle of the leading blade in the direction of rotation bordering the stalled passage is lower than what it is was designed for; this causes the passage to unblock. The incidence angle of the blades that are behind the stalled cell increases, thus these blades are stalled. Therefore the stall cell propagates and rotates in the opposite direction of the compressor rotation, but at a slower pace. A graphic explanation of this phenomenon can be seen in figure 2.6.
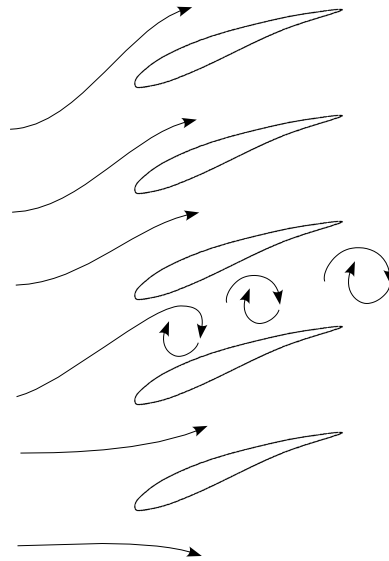


Figure 2.6: Graphic explanation on stall initiation

When stall occurs the blade row begins to vibrate due to the unsteady nature of the flow and the stall cell rotating in a blade row. If the compressor remains in the stall region for a period of time, it can be damaged, but not as excessively as it would have been if it was in the surge region. As a result, it is undesirable to operate a compressor in the stall region for long periods, but as mentioned previously it can operate in this mode. When stall occurs, a large pressure difference between the inlet and outlet is induced that can lead to surge.

The definition of surge is when a compressor does not compress the working fluid any more. While a compressor that is experiencing stall transfers the working fluid from the inlet to outlet, in surge the working fluid is pushed back through the inlet. Consequently the flow and pressure gradient inside the compressor can alter rapidly.

The conditions at stall and ultimately surge differ a great deal from the design conditions. Thus the condition is undesirable due to the fact that the blade rows of the compressor are working in an environment that they were not designed for. Surge effects the environment around the compressor due to the working fluid being forced through the inlet and outlet of the compressor. From this it is apparent that stall is a characteristic of the blade or blade row, whereas surge is a characteristic of the compressor system.

The maximum flow through a compressor is limited by a phenomenon called choke. It occurs when the inlet Mach number of the working fluid between two adjacent blades is increased to a point were the flow is sonic or supersonic. The speed of sound of the fluid depends on the relative stagnation pressure and temperature upstream of where the choke is located. Choking is also an undesirable condition for a compressor to operate at, but as the working fluid in this investigation is helium, choke will only happen in extreme cases that are not part of this study. However, a compressor can rather be operated at choke than stall or surge, because the blade rows vibrate during stall or surge.

## 2.4.2 Negative incidence stall

As mentioned in Section 2.1.2, the incidence angle is defined as the angle between the leading edge flow angle and blade angle. If the compressor is operated at high through-flow conditions the incidence angle becomes negative. Therefore the flow does not strike the leading edge of the blade at the intended design incidence angle. This will cause the flow to become separated much earlier than it is suppose to and cause the blade to experience negative incidence stall. Therefore, each blade has a specific design incidence angle that it should operate at.

Lieblein (1959) investigated the loading of cascades and developed the diffusion factor and equivalent diffusion factor. Lieblein only developed the so-called reference or design incidence angle, which occurs at the minimum loss incidence angle. The operating margin is defined as the incidence range where the pressure loss is less than twice the minimum pressure loss. Refer to figure 2.7 for a graphical explanation of this definition.

As can be seen in figure 2.7 the loss coefficient is fairly constant, however when the mass flow increases through the cascade, it starts to operate away from the design incidence angle, $i^*$, that is designed to be approximately zero. Thus the loss coefficient increases rapidly and the flow angle starts to differ from the blade angle, and the incidence angle starts to decrease and becomes negative. When the loss coefficient is twice that at design, the cascade operates at a negative incidence stall angle, $i_c$. This will cause the energy that the rotor adds to the flow to drop, and therefore the pressure rise per stage will decrease. Consequently the cascade will experience negative incidence stall. Conversely when the mass flow is decreased, the compressor will experience positive incidence stall, $i_s$. This investigation did not focus on the positive incidence stall region of the compressor, and this phenomenon will not be elaborated further.
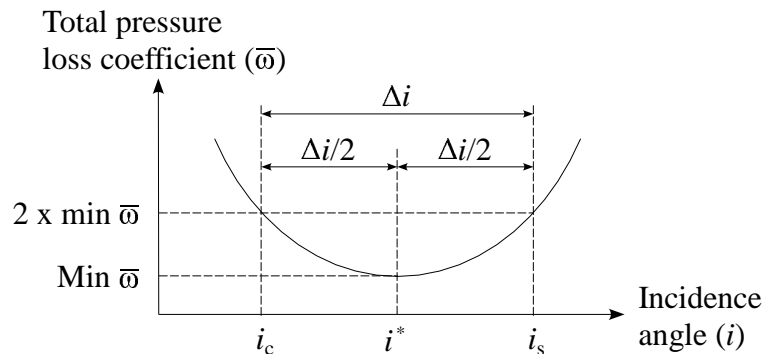


Figure 2.7: Definition of reference minimum loss incidence

It must be pointed out that, as mentioned previously, the theory of Lieblein is based on cascade data. It can be applied to an axial compressor, because it consists of blade rows that are arranged as cascades. However, negative incidence stall can occur in a cascade (blade row), but this does not mean that the compressor has stalled, especially if the stalled cascade is situated in the later part of the compressor. Consequently, the theory of Lieblein can be used to determine whether a compressor is experiencing negative incidence stall. If the stalled blade row is located at the inlet, the flow downstream will be distorted and therefore the later stages of the compressor could be stalled.

If the mass flow rate is increased even more, the outlet pressure of the compressor will become less than the inlet pressure. Thus the compressor will start to operate in the fourth quadrant (Section 2.5) and therefore as a turbine, extracting energy from the fluid.

## 2.5  Four-quadrant axial flow compressor maps

Each turbomachine has a design point where it operates at the optimum point. This point can be described as the sweet spot on the performance curve. This preferred point of operation is at a specific direction of rotation, flow direction and pressure difference across it. For a compressor, these operating conditions are all positive and the compressor operates in the first quadrant.

A graph can be drawn to illustrate the performance of a compressor, where the design point will be in the first quadrant where the pressure rise and flow rate is positive. A compressor or any turbomachine can be forced to operate at different operating conditions, thus in any four quadrants of a general graph. As described in Gill (2007), there are $2^3 = 8$ combinations of positive and negative flow, pressure rise, and rotational speed, but there are only four quadrants. It is thus clear that more than one mode of operation will occur in at least some quadrants.
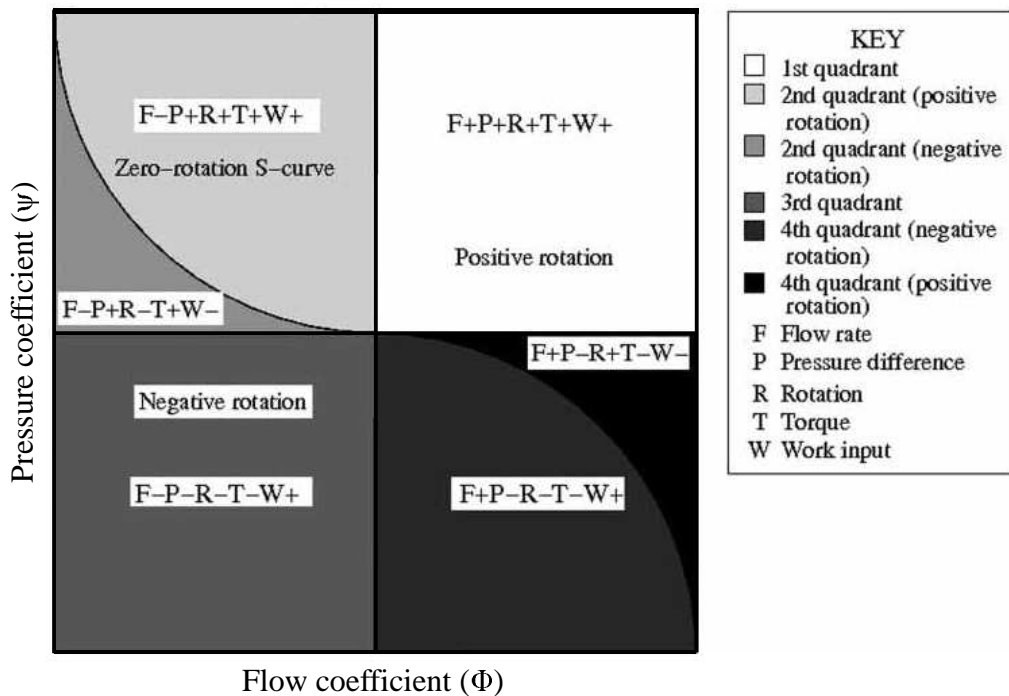


Figure 2.8: Generic four quadrant compressor map (Gill, 2007)

Refer to figure 2.8 for a generic four quadrant compressor map. The y-axis represents the static-to-static pressure coefficient, $\psi$, and is defined as follows: $\psi = (p_2 - p_1)/(1/2\rho U^2)$ where $p_2$ and $p_1$ are static pressures at the outlet and inlet, and $\rho$ is the density of the working fluid at the compressor inlet. The x-axis represents the flow coefficient, $\phi$, and is expressed as $\phi = C_x/U$, where $C_x$ is the average axial velocity at the inlet of the first stage of the compressor, and $U$ is the rotor blade tip speed. The zero-rotation S-curve defines the operating performance of a compressor with zero rotational speed, therefore the shaft is not rotating. The region above and to the right of the zero-rotation S-curve defines the region where the compressor is rotating in the positive direction. This will cause the pressure of the fluid to increase at a constant flow rate, or the other way around. With a positive rotor rotation, the compressor may operate in the first, second, or fourth quadrants. Similarly, the compressor can rotate in the negative direction, and therefore will operate to the left and below the S-curve. (Gill, 2007)

The normal operating region of a compressor is in the first quadrant, where the rotation and flow rate is positive and there is a pressure rise across it. If the flow rate is increased to such an extent that there is a pressure drop, the compressor is starting to operate in the fourth quadrant. The compressor will extract energy from the fluid and will operate as a turbine. The pressure coefficient of the compressor will become negative due to the pressure ratio across the compressor being less than one.

# Chapter 3

# Compressor Model

The purpose of this chapter is to familiarize the reader with the GTHTR300 compressor by giving some background information. It also contains the specifications and geometry of the compressor. The exact blade geometry of the GTHTR300 4-stage helium test compressor is confidential, thus a mathematical model was compiled to obtain the blade geometry and a brief description of the process is given, refer to Appendix A for a detailed description. The Stellenbosch University Rofanco 3-stage compressor was used as a test case to confirm if the mathematical model calculates accurate blade geometries.

## 3.1    Background information on GTHTR300 project

A nuclear reactor that utilizes steam turbines has a power generation efficiency of approximately 40%. As stated in Fujikawa *et al.* (2004), the typical temperature of a nuclear reactor is 950°C. On October 1st, 2005 the Japan Atomic Energy Research Institute (JAERI) and the Japan Nuclear Cycle Development Institute (JNC) were unified and become the Japan Atomic Energy Agency (JAEA). The JAEA undertook an investigation into nuclear helium gas turbines to exploit the properties of this gas at the high temperatures of a nuclear reactor. A prototype compressor was designed for a 300 MWe nominal-capacity power plant and is known as the GTHTR300 20-stage prototype compressor. A one-third scale test model of the prototype was designed along with a closed loop helium gas circuit for testing. The test model consists of four stages and are geometrically similar to the first four stages of the GTHTR300 prototype compressor.

The test rig operates with helium at mass flows up to 15 kg/s and using a 3.65 MW motor to drive the compressor. The maximum compressor inlet pressure is 1 MPa. The inlet temperature is controlled by a helium-to-water cooler. The test rig contains parallel valves to throttle the flow through the compressor to

20
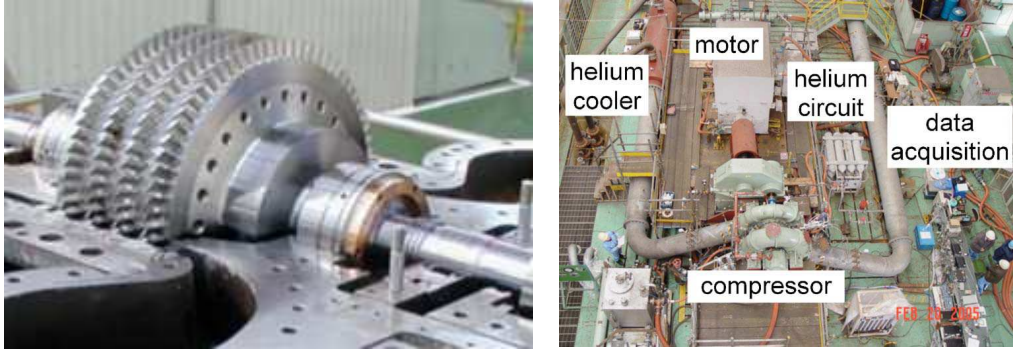
Figure 3.1: GTHTR300 4-stage helium test compressor and test rig

obtain the desired mass flow rate for each pressure ratio.  The GTHTR300
4-stage helium test compressor and test rig and can be viewed in figure 3.1.

## 3.2   Design conditions and aerodynamic specifications for the GTHTR300 compressors

In this section, the compressor geometry is given and discussed. Some of the
parameters given in Takizuka *et al.* (2004) and Yan *et al.* (2008) differed, there-
fore the most recent information was used as given in Yan *et al.* (2008).

This investigation modelled the 4-stage test model of the GTHTR300. See ta-
ble 3.1 for the specifications as obtained in Yan *et al.* (2008), unless otherwise
stated. The reason for choosing the test model and not the prototype was that
there is experimental data available for the 4-stage test compressor (Yan *et al.*,
2008) with helium as the working fluid.

The flow and load coefficients given in Yan *et al.* (2008) as shown in table 3.1
were not used in the calculations. The definitions as specified in Dixon (1998)
were applied to determine these coefficients, refer to equation (2.2.3) and equa-
tion  (2.2.4), respectively. This resulted in a flow coefficient of 0.47 and a load
coefficient of 0.30.  The flow coefficient is of the same order as given in  Yan
*et al.* (2008), but the load coefficient differs dramatically, probable due to
different definitions given for this coefficient.  Refer to Appendix A for the
calculations.

The relative Mach number at the rotor tip for the first rotor row is of the
order of 0.35 that is low (Cumpsty, 1989). The relative Reynolds number at
the tip is also low, $6.5 \times 10^5$. This makes the GTHTR300 4-stage helium test

Table 3.1: Design conditions and aerodynamic specifications of the prototype and test compressors

| Design conditions | | |
|---|---|---|
| | Prototype | Test model |
| Inlet temperature (°C) | 28.4 | 30 |
| Inlet pressure (MPa) | 3.52 | 0.883 |
| Pressure ratio, flange to flange | 2.0 | $1.156^1$ |
| Mass flow rate (kg/s) | 442 | 12.2 |
| Rated rotational speed (rpm) | 3600 | 10800 |
| Aerodynamic specifications | | |
| Number of stages | 20 | 4 |
| Tip diameter ($1^{st}/20^{th}$ stage, mm) | $1704/1645^1$ | $568/na^1$ |
| Hub diameter (mm) | 1500 | 500 |
| Boss ratio ($1^{st}/20^{th}$ stage) | $0.88/0.91^1$ | $0.88/na^1$ |
| Polytropic efficiency (%) | 90.5 | 88.7 |
| Rotor/stator chord length ($1^{st}$ stage, mm) | 78/60 | 26/20 |
| Rotor/stator blade height ($1^{st}$ stage, mm) | $102/101^1$ | $33.66/33.66^1$ |
| Rotor/stator solidity ($1^{st}$ stage) | 1.19/1.20 | |
| Rotor/stator aspect ratio ($1^{st}$ stage) | 1.3/ 1.7 | |
| Rotor tip/stator hub clearance | 1% blade span | |
| Peripheral speed of rotor blade ($1^{st}$ stage, m/s) | 321 | |
| Number of rotor/stator blades ($1^{st}$ stage) | 72/94 | |
| Flow coefficient | 0.51 | |
| Load coefficient | 0.63 | |
| Reaction | High reaction | |

compressor a very stable and easy compressor to simulate due to the absence of shock waves.

## 3.3 Blade geometry calculation

This section will explain the thought process followed to obtain the relevant blade angles that make up the blade profile geometries of the GTHTR300 4-stage helium test compressor. A was compiled to reverse engineer the he-

---

[1] Refer to Takizuka *et al.* (2004)

lium test compressor and is based on the methods described in Dixon (1998) and Aungier (2003). Refer to Appendix A for a detailed overview of the theory used to compile the mathematical model. Some assumptions were made to obtain the geometry, but they are fair and reasonable and can be justified. The assumptions that where made is given below.

The NACA 65-series blade profile with a maximum blade thickness to chord ratio, $t_b/c$, of 0.1 was used with a circular arc camber line. This blade profile is a common profile to use in a compressor of this nature with a low Mach number (Aungier, 2003).

To determine the blade profile geometry, the reaction ratio value had to be assumed, since the data given only states that it is high. Various simulations were conducted with a wide range of reaction ratio's, from 0.65 to 0.85. A reaction ratio of 0.8 at mid span gives the most accurate results when compared with the experimental data for the helium test compressor. This is considered as a high reaction ratio, therefore it confirms the aerodynamic specifications as specified in Yan *et al.* (2008) as given in table 3.1.

A constant hub diameter was assumed. From the pictures presented in Yan *et al.* (2008), it can be seen that this is a practical assumption. However, the casing wall has a slight taper. The gradient was calculated by taking the density ratio across the compressor and setting it inversely equal to the area ratio between the inlet and outlet. Refer to Appendix A for the calculations.

Normal stage loading was assumed. This is when any particular stage is geometrically similar to the preceding one. The fluid is turned towards the axial direction by the stator blade so that the flow enters the following rotor blade at the same angle as the inlet of the previous rotor, $C_1 = C_3$ and $\alpha_1 = \alpha_3$. This is a common design approach in axial compressor design and proved to be effective.

The gap between the rotor and stator blade row was made identical. The size of the gap was made equal to the average projected blade chord length with respect to the axial direction at the hub and spacing the blades by this length. This provided efficient spacing between the blade rows.

A free vortex design was implemented to calculate the angles at nine different lengths of the blade span for the helium test compressor. Other types of vortex design were investigated, namely the constant reaction and constant swirl vortex designs. The design pressure ratio predictions for the different blade design obtained using the different vortex designs were less than 2%. However the free vortex design gave the best results compared to the available experimental data and this vortex design is a common design principle used

in the design of axial compressors as stated in Aungier (2003). Consequently the blades that were used, were that using the free vortex design.

The axial velocity was assumed to stay constant along the blade span. This is not entirely true due to the end-wall boundary layers, but it simplifies the calculations. Due to the axial velocity not being exactly constant, it would have an effect on the calculations, but the error making this assumption will be acceptable. This assumption is used generally in compressor design and is a reasonable assumption.

What follows is an overview of the mathematical model used to calculate the blade geometry. Firstly the thermodynamic conditions of the compressor were calculated. From this the load and flow coefficients could be calculated. By using the reaction ratio, load coefficient and flow coefficient the flow angles could be obtained. The next step was to calculate the design incidence and deviation angles and design angle of attack by using the model of Lieblein (1960) with the correlations of Aungier (2003). The camber angle was estimated, because it was needed to calculate the design incidence and deviation angles and was taken initially as the difference between the relative flow angles. Therefore an iterative process was followed until the difference between consecutive camber angles was less than $1 \times 10^{-6}$. By using the design incidence and deviation angles, the blade angles could be obtained. With the blade angles known, the camber and stagger angles could be calculated.

A sensitivity analysis was done by Gill (2006) to investigate the effect of the boundary layer blockage model incorporated into the SUCC. There is an option to use the SUCC without the boundary layer blockage model, but it was concluded by Gill that the results without the model were inaccurate. Therefore, it was used in this investigation with a boundary layer of 1% for the hub and 1% for the shroud at the inlet. According to Aungier (2003), the inlet blockage is around 2% of the annulus area, thus 1% inlet blockage for the hub and shroud is a reasonable value to assume. The mathematical model was adjusted to factor in the inlet area being smaller due to the boundary layer blocking the flow. The inlet area in the mathematical model was made smaller by 2% and resulted in the axial velocity being higher.

## 3.4 Blade geometry of Rofanco 3-stage compressor

To verify if the mathematical model produces sufficient blade geometries, the blade geometries of the Rofanco 3-stage compressor of Stellenbosch University was calculated and compared to the exact blade geometries. The Rofanco

compressor is a low speed, low pressure ratio machine. The compressor is a low cost experimental test bench, but does not have the original plastic blades, as they were destroyed some years ago. The blades were redesigned by Benade (1987) and replaced by aluminium NACA 65-series blades with normal stage loading, resulting in three repeating stages. The compressor does not contain inlet guide vanes; therefore the reaction is relatively high being 0.82 at mid span. The design speed of the machine is 3000 rpm with a mass flow rate of approximately 3.5 kg/s. The nominal total-to-total pressure ratio across the compressor is of the order of 1.022. It is a very appealing test case to justify the mathematical model, as the geometry is very straightforward and similar to the helium test compressor. The only significant difference is that the helium test compressor has an extra stage.

Table 3.2: Exact and calculated rotor and stator blade angles of the Rofanco compressor

| Fraction of Blade Span | Exact Geometry | | Calculated Geometry | |
|---|---|---|---|---|
| Rotor | Stagger (°) | Camber (°) | Stagger (°) | Camber (°) |
| 0.00 | 38.00 | 31.04 | 41.79 | 23.36 |
| 0.25 | 45.00 | 23.48 | 46.59 | 18.81 |
| 0.50 | 49.40 | 17.93 | 50.47 | 15.43 |
| 0.75 | 53.00 | 13.85 | 53.67 | 12.88 |
| 1.00 | 56.10 | 10.90 | 56.36 | 10.91 |
| Stator | | | | |
| 0.00 | 20.38 | 46.28 | 16.73 | 38.62 |
| 0.25 | 18.18 | 43.49 | 15.80 | 36.71 |
| 0.50 | 16.61 | 41.05 | 14.94 | 35.00 |
| 0.75 | 14.90 | 40.57 | 14.15 | 33.46 |
| 1.00 | 14.32 | 40.00 | 13.42 | 32.07 |

Refer to table 3.2 for a comparison between the exact and calculated blade angles. The exact blade angles where obtained from Benade (1987). The relevant rotor blade angles of the Rofanco compressor is similar to that calculated using the mathematical model, except at the hub where the camber angles are much larger, by approximately 8°. The reaction at mid span for the calculated blades is the same as the exact blades at 0.82.

## 3.5   Blade geometry of GTHTR300 4-stage helium test compressor

The relevant blade angles of the GTHTR300 4-stage helium test compressor can be viewed in table 3.3. As mentioned previously nine points were calculated, but only five are shown for simplicity. With the blade angles now available, the test compressor could be analyzed to obtain the performance characteristics.

Table 3.3: Calculated rotor and stator blade angles of the GTHTR300 4-stage helium test compressor

| Fraction of Blade Span | Calculated Geometry | |
|---|---|---|
| Rotor | Stagger (°) | Camber (°) |
| 0.00 | 50.75 | 18.95 |
| 0.25 | 52.33 | 17.37 |
| 0.50 | 53.77 | 15.97 |
| 0.75 | 55.10 | 14.74 |
| 1.00 | 56.33 | 13.64 |
| Stator | | |
| 0.00 | 20.13 | 42.67 |
| 0.25 | 19.75 | 42.02 |
| 0.50 | 19.38 | 41.38 |
| 0.75 | 19.01 | 40.76 |
| 1.00 | 18.66 | 40.16 |

# Chapter 4

# 2-Dimensional Simulation Results

In this chapter the results of the 2-D simulations obtained from the SUCC will be shown and discussed. A summary of the stall and loss models included in the SUCC are presented. Using the mathematical model to obtain the blade profile geometry, the performance results for the Rofanco 3-stage compressor and also those of the GTHTR300 4-stage helium test compressor could be predicted. The Rofanco compressor was used as a test case to verify the mathematical model. A summary is given for each computational grid and boundary layer. The chapter concludes with a summary of the results.

The South African Air Force needed a computer code that could model the performance of axial flow compressors in certain gas turbine engines, as part of an engine life extension program. The code had to generate axial flow compressor maps consisting of pressure ratio or efficiency versus flow characteristics for various rotating speeds. Therefore the SUCC was developed by Thiart (2004). The code uses axisymmetric inviscid throughflow methods with boundary layer blockage and empirical blade row loss models. Furthermore, Gill (2006) added a number of stall prediction criteria to the SUCC.

## 4.1   Models incorporated into the SUCC

The stall models implemented into the SUCC by Gill (2006) were the diffusion factor criterion, de Haller's criterion, Aungier's blade row, boundary layer and system stability criterion, a simplified version of Dunham's stability criterion and a similar static-to-static stability criterion. Each model is described mathematically, and the algorithm used to implement it in to the SUCC is presented in Gill (2006).

The efficiency that SUCC predicted was higher than the experimental values, but the SUCC did not contain the blade tip clearance loss model as described in Section 2.3.1. Therefore, it was added to the CompressorBladerows module

27

of the SUCC to improve it with the aid of Gill (2009) who has considerable knowledge on the internal workings of the SUCC. A standard 1% of the blade span tip clearance is used for the rotor and stator blades. The efficiency dropped in the order of 2.5% and came within 2% of the experimental values. This is a very good improvement and made the code more accurate.

The code can be further improved by adding more loss models. The shock wave loss models as explained in Aungier (2003) is not included in the SUCC. It can be added, but will not be required in this case as the relative Mach numbers at the tips of the helium and Rofanco compressors are low, in the order of 0.35 and 0.2, respectively. However, it would be essential if the compressor has a high Mach number where sonic flow is likely to take place.

As mentioned previously, the model described in Section 2.3 and discussed in Appendix B is implemented in the Aungier module of the SUCC. This accounts for off-design operating conditions where negative and positive incidence stall may occur as explained in Section 2.4.2.

The boundary layer blockage model incorporated into the SUCC is that of Aungier (2003). A blockage value is assigned at the inlet for the hub and shroud. The wall shear stresses are calculated and from this the meridional momentum thickness and tangential momentum flux thickness. From this the boundary layer thickness can be calculated. This process is repeated for each meridional station until all stations have been analyzed.

## 4.2 Convergence criteria, relaxation factors and computational times

The SUCC implements two simulation methods, namely the Matrix Through Flow Method (MTFM) and the Streamline Curvature Method (SCM) (Cumpsty, 1989). The MTFM was used to simulate both compressors, thus the focus will be on this method. The SCM was also applied, but the MTFM gave better and more stable results. The convergence criteria used for the MTFM is that the normalised maximum change in the stream function at all points on the computational grid, should not exceed the convergence tolerance at $10^{-5}$. This value could have been made lower, but no noticeable loss in accuracy was observed, and it allowed a considerable saving in computational time. The boundary layer blockage modelling method in the SUCC was utilized. This model's convergence tolerance is set at $10^{-4}$. It is impractical to lower this value, as there appeared to be a limit on the accuracy of the boundary layer method not far below this value.

The relaxation factors used for the MTFM simulations were 0.1. Although this value is low it improves the stability of the process. This value was sometimes increased to 0.3 for the Rofanco, but the most stable simulations for the test compressor were obtained with the former value. The relaxation factor for the boundary layer modelling method is slightly smaller. The value was set at 0.08 for both compressors.

All simulations were performed on a Pentium D, 2.80 GHz computer with 2.0 GB of RAM. The computational time for both compressors is approximately five seconds per mass flow rate doing 500 iterations. To determine the performance curve of the compressors, it is equal to the number of working points times the computational time. The compressors were simulated from 70% to 130% design mass flow rate; therefore each run took about 5 minutes to complete.

## 4.3   Rofanco compressor

The computational grid used for the Rofanco compressor test case is shown in figure 4.1. The SUCC contains the geometric data for the Rofanco as an example. This geometric data was measured by several researchers that worked on the Rofanco, including Lewis (1989), Roos (1990), Roos (1995) and Gill (2006). Quasi-orthogonals are used in SUCC to define the space that each blade row occupies in the annulus. A quasi-orthogonal was placed as close as possible to the leading and trailing edge of each blade row. If the quasi-orthogonal is placed outside the blade row, the SUCC does not work. Five quasi-normals that define the grid were placed between the inlet and leading edge of the first blade row, and five between the last blade row trailing edge and the outlet. The blades or quasi-orthogonals are indicated by the slightly thicker dotted lines. Due to the Reynolds number being fairly low, the number of streamlines could be reduced to simplify the computation time. Five streamlines were chosen and the accuracy did not improve by increasing the number of streamlines.
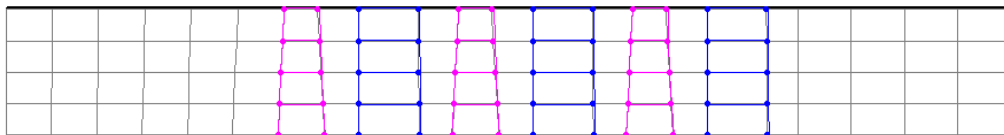


Figure 4.1: The SUCC model of the Rofanco compressor

The Rofanco was simulated with an inlet pressure of 101325 kPa and temperature of 27°C at the design mass flow rate of 2.66 kg/s. The experimental data

was obtained from Gill (2006), Roos (1990) and Roos (1995). See figure 4.2 for the pressure map of the Rofanco compressor at 100% design speed. The design point is at a pressure ratio of approximately 1.022 and mass flow rate of 2.66kg/s.
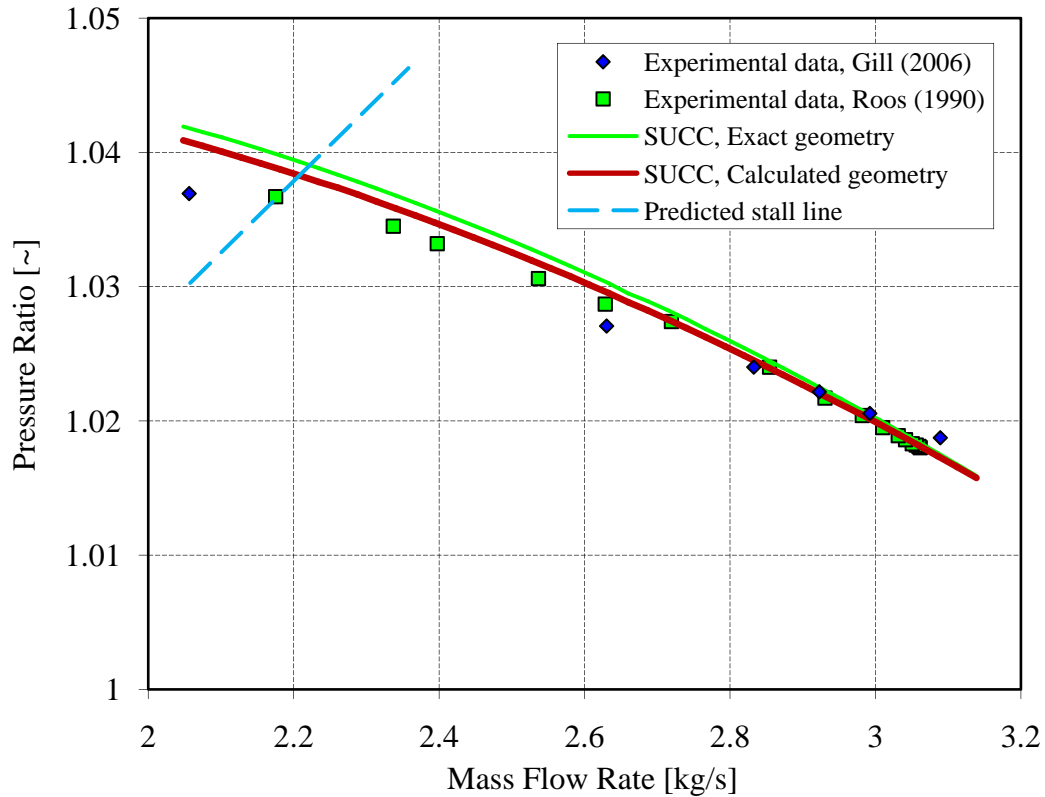


Figure 4.2: Pressure vs. flow performance for the Rofanco compressor using the SUCC

According to Gill (2006), the only stall criterion that gives accurate stall predictions at low Reynolds number are the de Haller stall criterion. The SUCC predicted stall in the compressor, according to the de Haller stall criterion below 83% design mass flow rate. The indicated stall line was slightly conservative, but offered reasonable agreement with the experimental stall limit that is roughly on the same point, 79%. The Aungier and the diffusion factor stall criteria did not predict stall in the compressor.

The SUCC predicts the total-to-total pressure ratio for each percentage design mass flow rate. The pressure ratio prediction was within 1% compared to the experimental data. That is considered to be satisfactory and confirmed that the mathematical model could be used to calculate the blade profile geometries of the GTHTR300 4-stage helium test compressor. This prediction also shows

that the SUCC can be used to simulate an axial compressor, except in the stall region were the accuracy is not adequate.

## 4.4    GTHTR300 4-stage test compressor

The computational grid used for the GTHTR300 4-stage test compressor is shown in figure 4.3. The geometry of this compressor is similar to the Rofanco compressor, therefore the same computational grid setup was used. The compressor geometry, excluding the blade profiles, was obtained from Yan *et al.* (2008). The simulations were done only at design speed, because the experimental data obtained from Yan *et al.* (2008) is at this speed. The simulations were performed using the MTFM with the boundary layer blockage model. The boundary layer was chosen as 1% for the hub and shroud at the inlet.
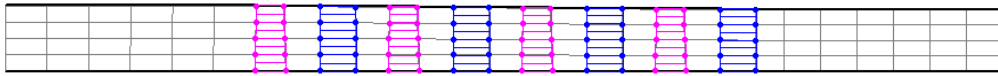


Figure 4.3: The SUCC model of the GTHTR300 test compressor

Two sets of experimental data for the GTHTR300 4-satge helium test compressor were taken from Yan *et al.* (2008). The first was performed at a nominal inlet pressure of 0.896 MPa and inlet temperature of 28.7°C and the second at 0.543 MPa and 26.9°C. The helium test compressor was simulated at the design conditions, that is at an inlet pressure of 0.883 MPa and 30°C at a mass flow rate of 12.2 kg/s. See figure 4.4 for the pressure map and figure 4.5 for the adiabatic efficiency map of the GTHTR300 4-stage helium test compressor. The design point is at a pressure ratio of approximately 1.17 and mass flow rate of 12.2kg/s.
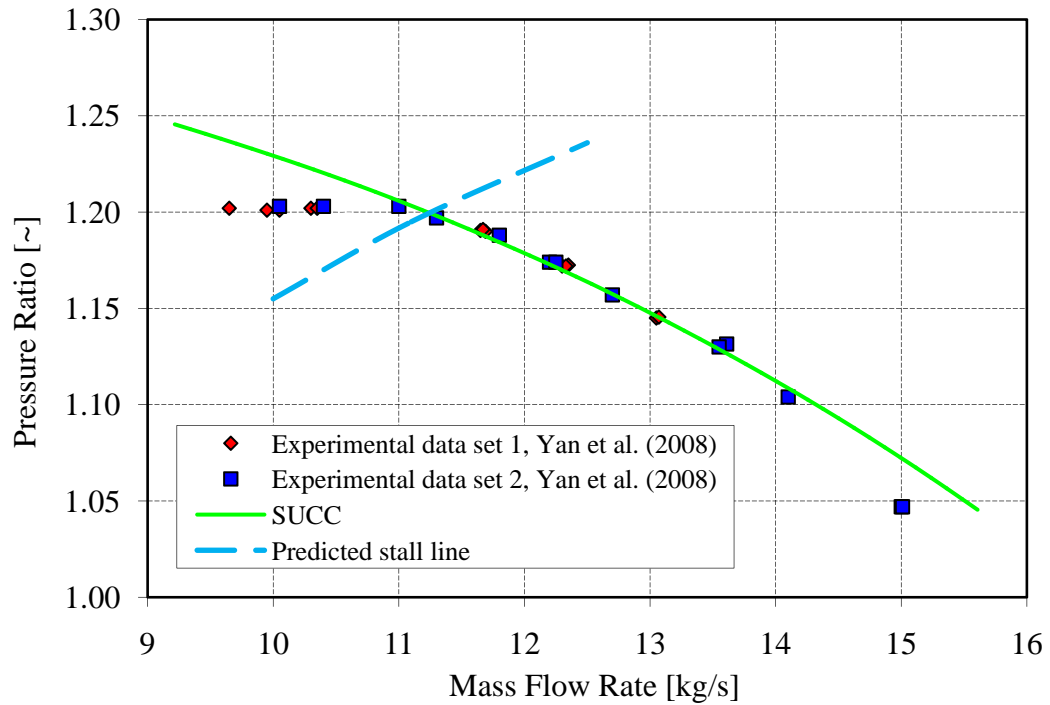
Figure 4.4: Pressure vs. flow performance for the GTHTR300 4-stage helium test compressor using the SUCC

The SUCC predicted stall in the compressor according to the de Haller stall criterion below 91% design mass flow rate. This is a higher mass flow rate than the Rofanco 3-stage compressor, however the stall margin is exactly the same as the predicted and observed in Yan *et al.* (2008). The pressure ratio prediction compare adequately with the experimental data with an error of less than 1% for the design point. The adiabatic efficiency prediction for the design point is within 2%. This is a very good approximation of the adiabatic efficiency for the SUCC compared to the results obtained by Gill (2006) for the NACA 5-stage and 10-stage compressors. Therefore, adding the blade tip clearance loss model as described in Section 2.3.1 did improve the code.

Figure 4.5: Efficiency vs. flow performance for the GTHTR300 4-stage helium test compressor using the SUCC

A sensitivity analysis was done to see what effect the boundary layer has on the compressor performance. The blade geometry that was calculated for an inlet boundary layer blockage of 1% represents the experimental data adequately as shown in figure 4.4 and figure 4.5. To further illustrate the effect of boundary layer blockage, the compressor was simulated at other blockage values. It was simulated at a boundary layer blockage of 2% and 4% for the hub and shroud at the inlet. A boundary layer blockage value of 4% is very high for the inlet of an axial compressor, but it is used here to illustrate the effect that it has on the performance. The results of these simulations can be viewed in figure 4.6 for the pressure ratio performance and the adiabatic efficiency performance in figure 4.7.

It can be seen from figure 4.6 and figure 4.7 that the boundary layer blockage does influence the performance of a axial compressor. Therefore, during the reverse engineering of the blade geometries the boundary layer was incorporated into the mathematical model, refer to Section 3.3. The results show that the mathematical model does produce blade geometries that accurately predict the experimental data if the compressor is simulated at the intended design conditions. When a compressor is simulated at other boundary layer blockage values that it was not designed for, the results deviate from the experimental data. Thus the blockage value must be taken into account.
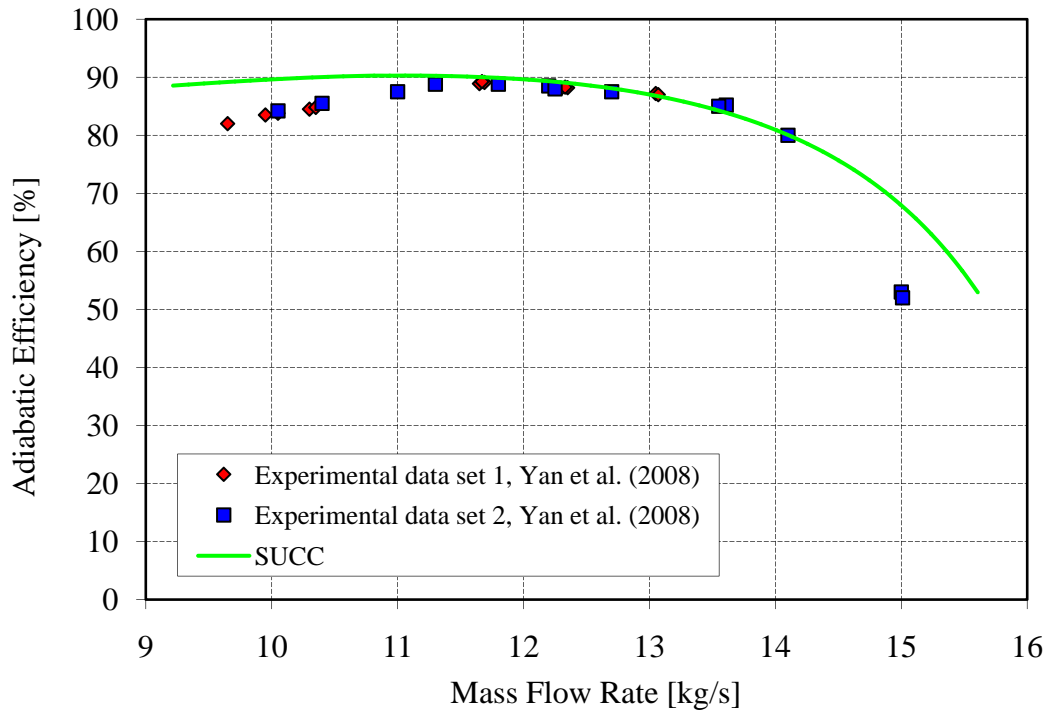
Figure 4.6: Pressure vs. flow performance for the GTHTR300 4-stage helium test compressor using the SUCC with various blockage values

An interesting observation is that the results deviate by a constant margin if the compressor is simulated at other blockage values. If the blockage is increased, the pressure rise per stage decreases. This is due to the boundary layer reducing the area the fluid can flow through. This causes the mass flow and axial velocity to increase and therefore the pressure ratio drops. This effect starts to play a much bigger role when the mass flow rate is increased. Then the boundary layer becomes larger and more prominent in the later stages of the compressor.
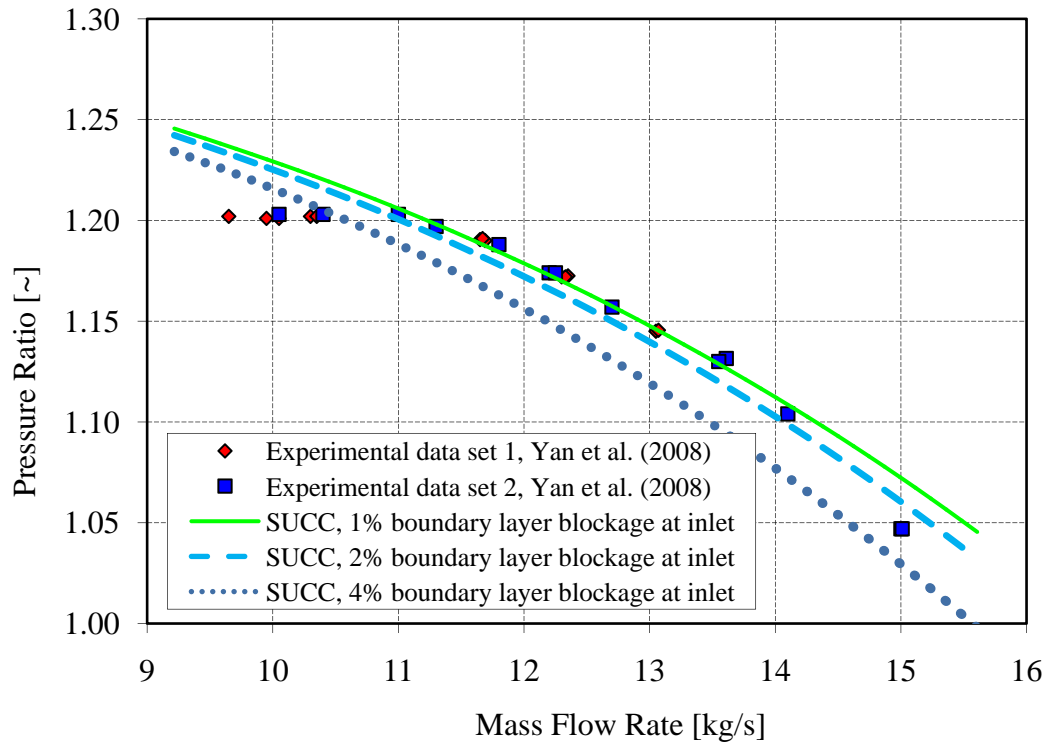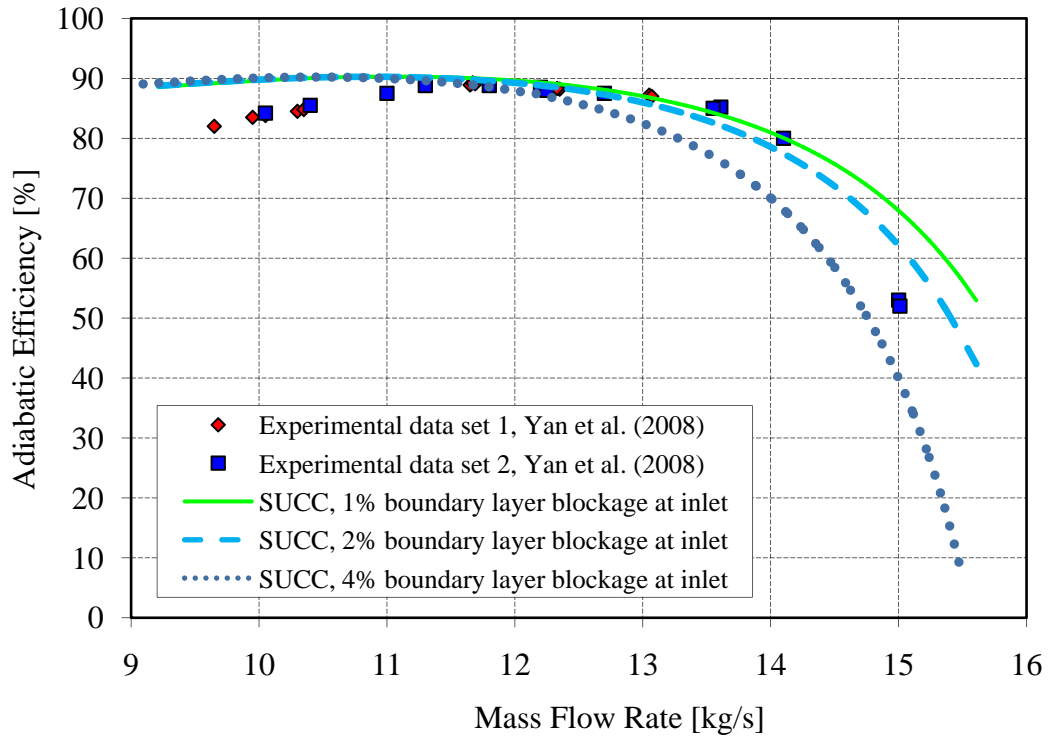
Figure 4.7: Efficiency vs. flow performance for the GTHTR300 4-stage helium test compressor using the SUCC with various blockage values

## 4.5 Summary of results

This chapter has described the results of the simulations of the Rofanco 3-stage compressor as a case study and the GTHTR300 4-stage helium test compressor.

The pressure ratio predictions of the Rofanco compressor agreed adequately compared to the experimental data of Gill (2006)and Roos (1990) with an error of less than 1%. Therefore the mathematical model could be used to calculate the blade geometries for the helium test compressor. The predictions also indicate that the SUCC can simulate an axial compressor with reasonable accuracy.

The pressure ratio prediction of the helium test compressors was within 1% for the design point compared to the experimental data of Yan *et al.* (2008). The adiabatic efficiency prediction was considered to be accurate with an error of 2%.

Stall was predicted in both compressors by the de Haller criterion and the prediction is at the same point were it was observed in the experiments. However, the pressure ratio predictions of both compressors at low mass flow rates and high pressure ratios are not accurate. This may perhaps be due to the low

Reynolds number effect which is not included in the SUCC. By adding a low Reynolds number model the stall point can be better predicted, but the overall accuracy is acceptable.

The adiabatic efficiency that SUCC predicted was high, but the SUCC did not contain the blade tip clearance loss model as described in Section 2.3.1. Therefore it was successfully added to improve the code and the efficiency prediction came within 2% of the experimental data.

There is some deviation in both the pressure ratio and efficiency predictions at mass flow rates higher than design. This may be because the SUCC is an axisymmetric inviscid throughflow code that does not take the viscous effect into account.

The boundary layer model was investigated to determine its effects on the blade geometry design. It was concluded that this value must be kept to a minimum, thus a value of 1% is realistic for the inlet blockage at both the hub and shroud.

# Chapter 5

# 3-Dimensional Simulation Results

In this chapter the results of the 3-D simulations obtained from NUMECA FINE™/Turbo version 8.7-2 will be shown and discussed. Only the GTHTR300 4-stage helium test compressor was investigated as it is the focus of the research topic. A summary is given for the computational grid, turbulence model parameters and boundary condition. The chapter concludes with a summary of the results.

## 5.1 Computational model information

This section gives some background information into the Computational Fluid Dynamics (CFD) software used in this investigation. The boundary conditions, turbulence model and computational time and resources are discussed. The quality of the mesh is given and discussed.

CFD solves the Navier-Stokes equations by using numerical methods and algorithms. When the flow is turbulent it can be solved using Direct Numerical Simulation (DNS). This method captures all of the relevant vortices of turbulent motion. This approach is extremely expensive for complex problems on modern computing machines, hence the need for models to represent fluid flow economically. A typical two-equation turbulent model implements length scales and turbulent intensity values to modify the Navier-Stokes equations. CFD has become sophisticated and widely used in product development (Horlock and Denton, 2005). It has become possible to simulate turbomachinery in three dimensions that takes viscous effects into account, as in Pratap and Geetha (2005). Furthermore, time dependant simulations can be performed, such as in Grüber and Carstens (2001). Time dependent simulations was not performed, due to the resources and computational time required.

In addition to the 2-dimensional investigation that was done to establish a blade geometry, as described in Section 4.4, CFD was used to gain further and

better knowledge of the helium test compressor. NUMECA FINE™/Turbo was used and is a 3-dimensional multistage viscous solver extensively used in the turbomachinery industry.

AutoBlade™ of NUMECA was used to generate the computational mesh. This is an advanced and effective modeller dedicated to the design of turbomachinery blades. It uses hexahedral type cells that can be optimized to improve the orthogonality of each cell. The computational model is constructed of structured H-mesh intersected by streamwise, quasi-orthogonal, and meridional surfaces. The CFD model for the helium test compressor is shown in figure 5.1.
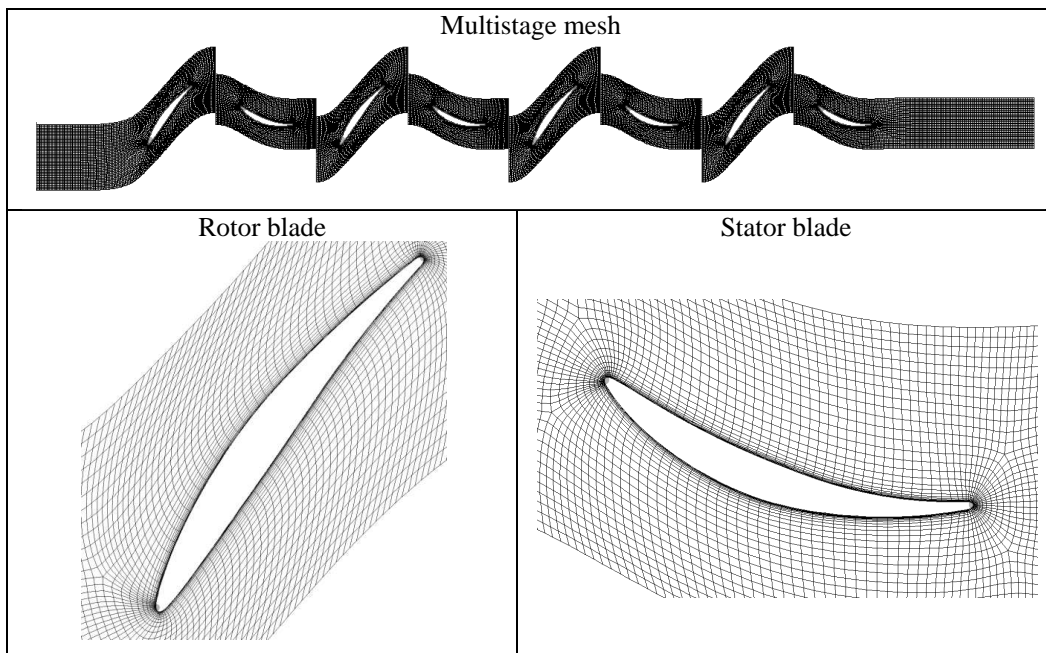


Figure 5.1: CFD model of the GTHTR300 4-stage test compressor

NUMECA FINE™/Turbo refines the mesh by means of a *multigrid scheme.* The mesh is contracted in AutoBlade™. The mesh is constructed at the finest setting that is named the *multigrid level* and is indicated as 0, 0, 0 for the i, j and k direction, respectively. However to shorten computation time, the simulations are run at a course *multigrid level*, namely 2, 2, 2. The results for this simulation are then used for the next simulation that is done at a finer *multigrid level*, namely 1, 1, 1. The mesh refinement can be seen in figure 5.2.

The mesh count is 89 streamwise, 41 pitchwise, and 61 spanwise elements per blade. This gives a very good quality mesh for both the rotor and stator blades. The number of streamwise points at the inlet and outlet is 61, which
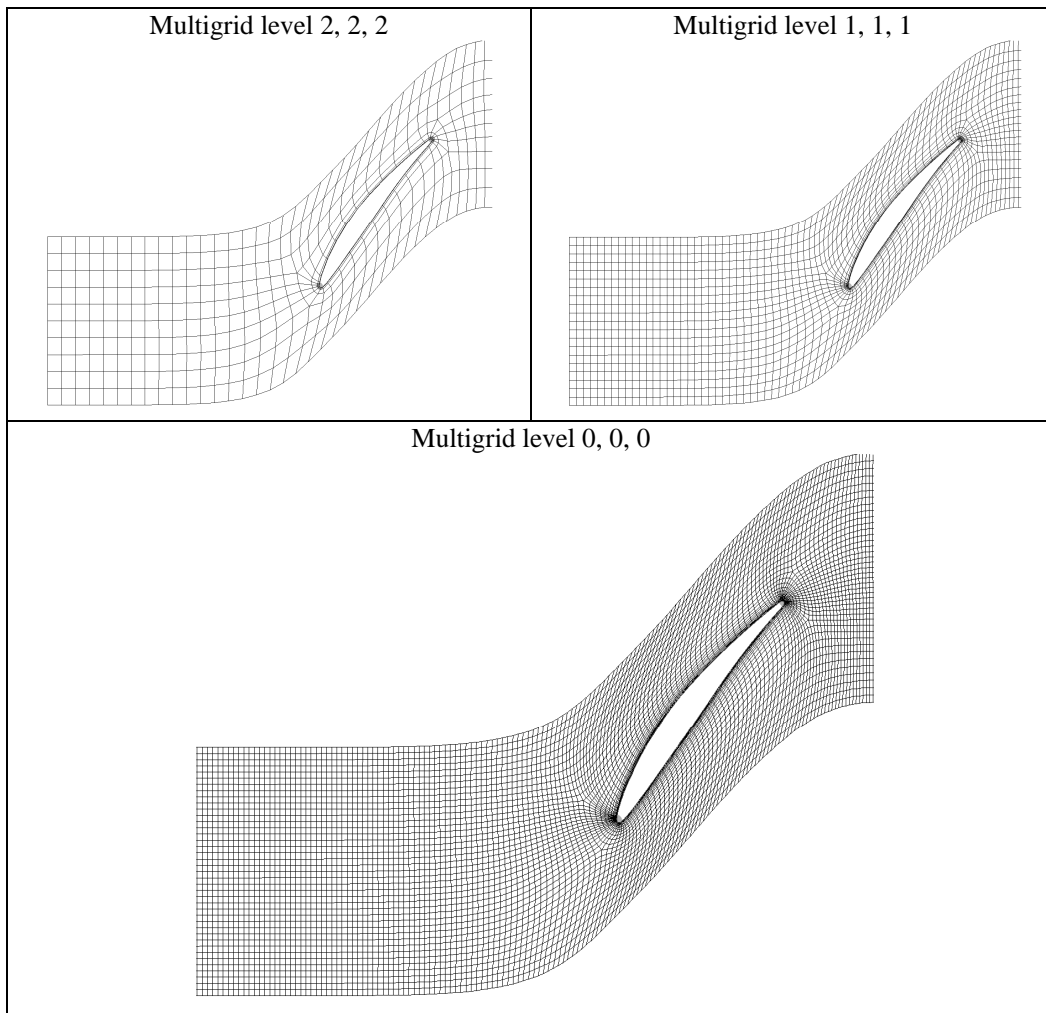
Figure 5.2: Multigrid levels for the first rotor of the GTHTR300 4-stage test compressor

gives a smooth transition to and from the blade row. Out of the spanwise mesh count, 17 are in the clearances of the rotor tip and stator hub. The shroud and hub clearances are 1% of the blade span, therefore 0.34 mm. The adjacent blade rows assume computational interfaces with mixing planes. Full matching periodicity was applied between blades. The mesh was optimized for highly staggered blade rows and free inlet and outlet angles. The overall quality of the mesh was acceptable, see table 5.1 for a summary with the limits included. The mesh was optimized to improve the orthogonality of each cell. Roughly 220 optimization steps were used for the rotor blades and 100 optimization steps for the stator.

The 3-dimensional mesh can be seen in figure 5.3 showing all four stages of the test compressor. The total cell count is roughly 3.3 million cells and is based

Table 5.1: Overall CFD mesh quality of the GTHTR300 4-stage test compressor

| Parameter | Limits | Value |
|---|---|---|
| Minimum orthogonality | $> 18°$ | $22.8°$ |
| Maximum aspect ratio | $< 2500$ | $165.3$ |
| Maximum expansion ratio | $< 2.2$ | $1.87$ |
| Angular deviation | $< 600$ | $0.2$ |

on the number of cells that occupy one blade in each row (blade passage), see the top left-hand corner of figure 5.3. The mesh was refined to investigate the effect that it would have on the results. The cell count was doubled and therefore the computational time also increased by the same amount, but the total-to-total pressure ratio prediction changed less than 1% for the design
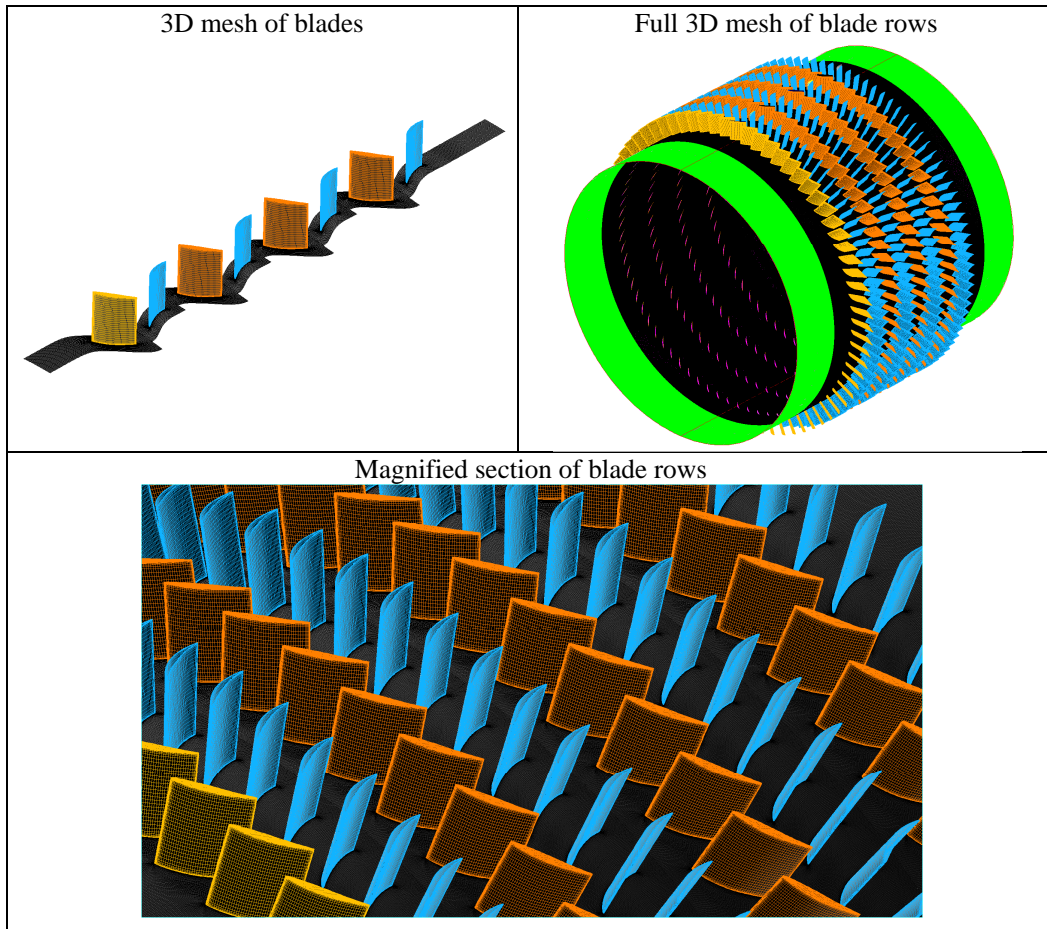


Figure 5.3: Full 3D CFD model of the GTHTR300 4-stage test compressor

point. Thus the mesh does not need to be refined for this type of investigation were numerous simulations are needed to obtain a performance map.

Steady state simulations were performed by using the Spalart-Allmaras turbulence model. This is a good model to use when simulating turbomachinery and gives adequate results. The inlet conditions were set at the design conditions, thus a pressure of 0.883 MPa and temperature of 30°C. The boundary conditions at the inlet were set using the total quantities imposed condition, with the velocity direction specified as axial. A turbulent viscosity of $1 \times 10^{-4}$ m$^2$/s was used. The outlet boundary conditions were set using the mass flow imposed condition with a pressure adaption set at 12.2 kg/s and initial pressure of 1 MPa. The performance maps were obtained by changing the outlet mass flow rate.

The mesh was refined and adapted so that the y$^+$ value for both blades were between 2 and 10 at the design point. This range of y$^+$ values is within acceptable limits for the Spalart-Allmaras turbulence model. The y$^+$ value at the leading edge is the highest, due to the curvature and the high velocities in this region.

The Stellenbosch University High Performance Computer (HPC) was used for the simulations. With two cores operating at 2.8 GHz, the simulations converged with mean density residuals between $-3 \times 10^{-3}$ and $-5 \times 10^{-3}$ in 46 hours or approximately 2 days with 6000 cycles. The time needed for convergence depends on the load of the cluster and where the compressor was being simulated. In the stall region the simulation took very long to converge due to the unsteady nature of the flow in this region. The computational load was balanced between the amount of cores and each core used about 1.8 GB of RAM.

## 5.2  GTHTR300 4-stage test compressor

This section discusses the performance of the GTHTR300 4-stage helium test compressor. See figure 5.4 for the pressure map and figure 5.5 for the adiabatic efficiency map. The design point is at a pressure ratio of approximately 1.17 and adiabatic efficiency of roughly 88% at a mass flow rate of 12.2kg/s.

As can be seen from figure 5.4 the FINE™/Turbo total-to-total pressure ratio prediction predicted the design point within 1%. At higher mass flow rates, the 3-dimensional results follow the same tendency as the experimental results, especially at mass flow rates higher than 15 kg/s. Another observation is that neither the SUCC nor FINE™/Turbo could accurately simulate the experimental point at roughly 15kg/s. However, the overall pressure ratio predictions
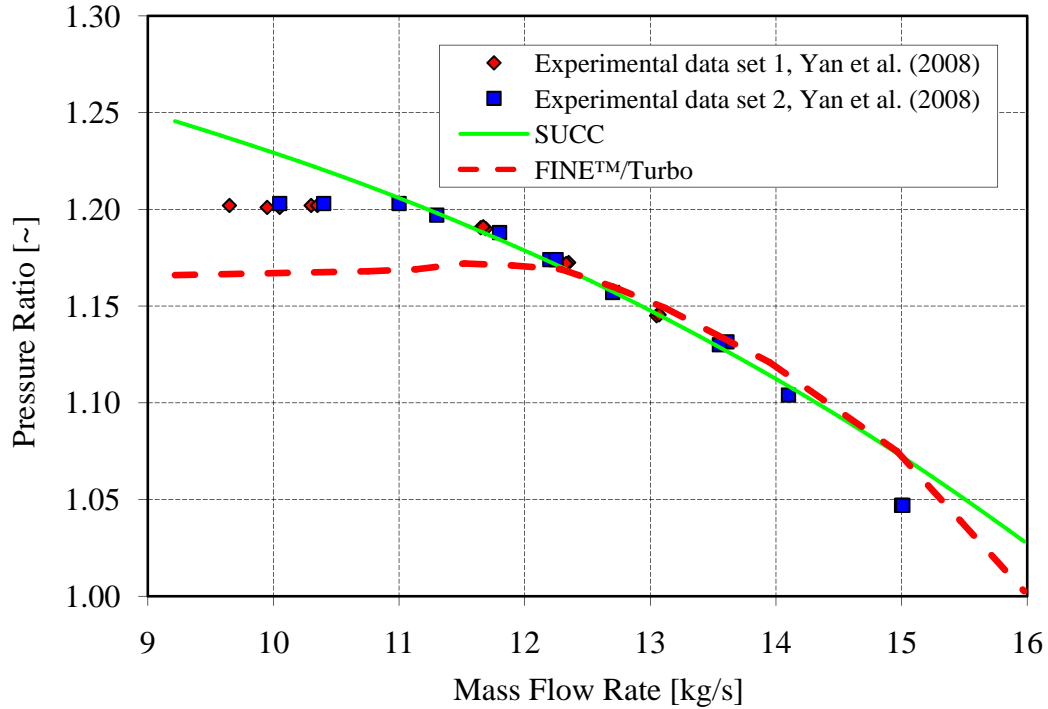
Figure 5.4: Pressure vs. flow performance for the GTHTR300 test compressor using NUMECA FINE™/Turbo

are very good for this type of investigation with limited information on the helium test compressor.

As the mass flow decreases the pressure ratio predictions become inaccurate as can be seen in figure 5.4. The 3-dimensional simulations do predict the stall region with a zero gradient on the pressure ratio performance map, something that the SUCC could not do. This also justifies simulating a compressor in 3-dimensions. The reason for the deviation in the results for mass flow rates lower than the design condition is due to the modelling technique. Only one blade passage was simulated and not the entire blade row. This is not an accurate method when simulating a compressor in the stall region where stall cells are present between the blades in a blade row. To accurately simulate a compressor in the stall region all the blades in a blade rows has to be taken into account. These simulations are a very resource intensive and time consuming and were not considered for this investigation.

The adiabatic efficiency prediction for the design point is within 4% as can be seen in figure 5.5. This is sufficiently accurate in CFD analysis of this kind as mentioned by Yan *et al.* (2008). The efficiency results predict the experimental data less adequately at mass flow rates higher than the design point, but deviates by a constant in the stall region.
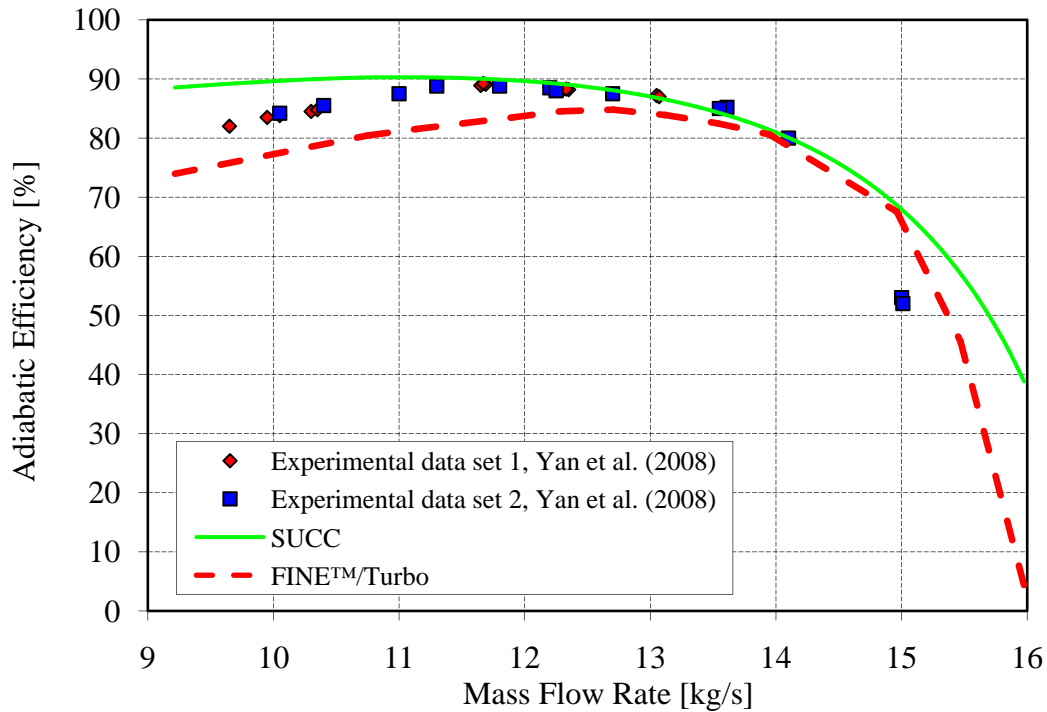
Figure 5.5: Efficiency vs. flow performance for the GTHTR300 test compressor using NUMECA FINE™/Turbo

To determine whether the rotor or stator blades were experiencing negative incidence stall, the flow velocities and angles were taken from the 3-dimensional simulations. The average data was taken upstream and downstream of each blade row by using NUMECA CFView™ version 8. CFView™ is the flow visualization and post-treatment package of NUMECA. The incidence angle at mid span for the rotor blade was 0.37° at design conditions. However, if the mass flow rate was increased to 16 kg/s (130% design mass flow rate) the incidence angle for the rotor blade became negative, -5.1°. The reason why it was taken at this high mass flow rate is that this is the extreme point were the pressure ratio is just above one at 1.003. This is also the point were the SUCC and FINE™/Turbo performance predictions deviated. According to the off-design cascade performance correlation of Aungier (2003), which is the loss model incorporated into the SUCC, the rotor blade was within the accepted limits. The limit is defined where the loss coefficient is less than twice the minimum loss coefficient. Refer to Section 2.3 for an overview and Appendix B for a detailed description of the off-design performance correlation. See Appendix C for a sample calculation to identify if a blade row is experiencing negative incidence stall. Negative incidence stall will initiate in the rotor blade if the compressor is operated in the fourth quadrant. To investigate the compressor in this region was not part of the scope for this thesis.
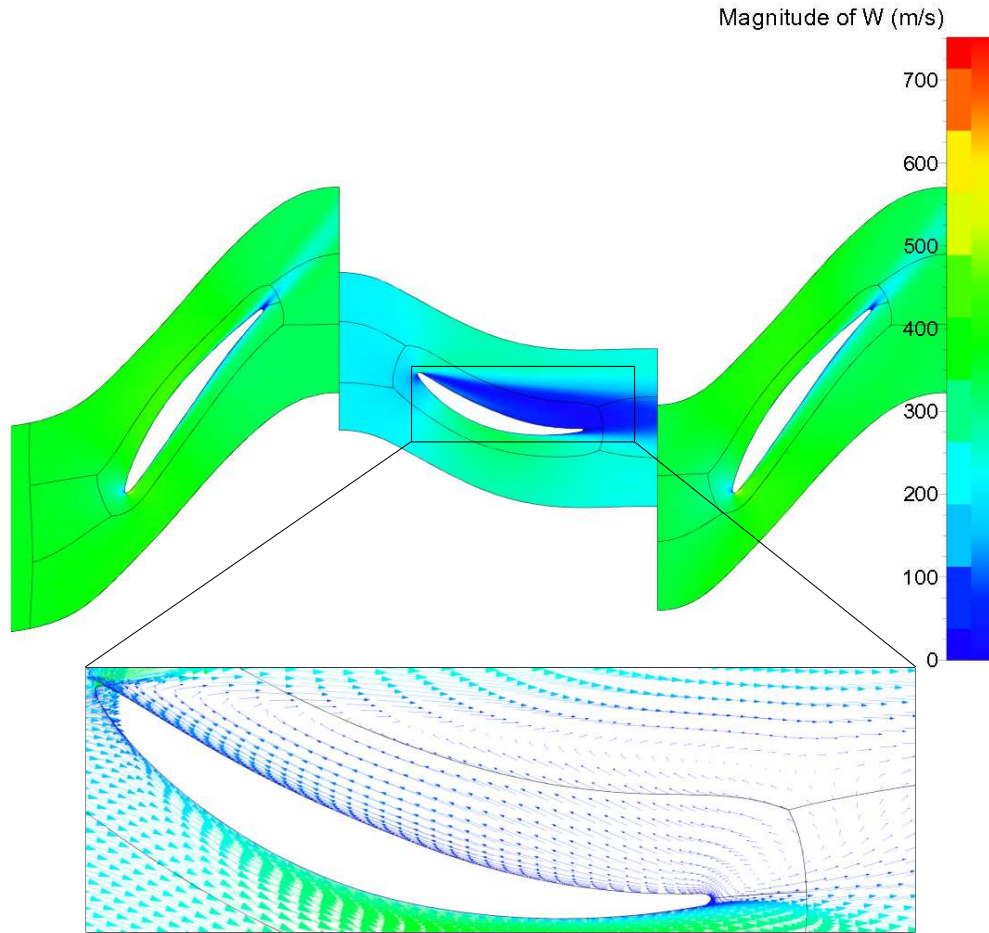
Figure 5.6: Relative velocity flow distortion behind stator blade

For the stator blade the incidence angle at mid span was -0.57° at design conditions. When the mass flow was increased to the same value as mentioned above (16 kg/s), the incidence angle at mid span was found to be -20.7°. Figure 5.6 shows the relative velocity magnitude and direction and from this it can be seen that there is a very large wake behind the stator blade with the flow recirculating. Thus the flow does not strike the blade at the intended design angle, resulting in the large incidence angle. From this it could be concluded that the stator blade row was experiencing negative incidence stall. This was confirmed by using the off-design cascade performance correlation. The loss coefficient was in the parabolic region of the loss bucket, but was outside the minimum loss limit as explained in the previous paragraph. If linear harmonic simulations were performed the effect of the wake behind the stator blade on the flowing rotor blade would have been simulated, especially if the mass

flow was increased beyond 16 kg/s. However, linear harmonic simulations are computationally expensive to perform and were not considered for this investigation. The reader is referred to Gill *et al.* (2009) who investigated an axial compressor and performed linear harmonic simulations at very high mass flow rates.

## 5.3   Summary of results

This chapter has described the results for the 3-dimensional simulation of the GTHTR300 4-stage helium test compressor. The 3-dimensional simulations were performed to further justify the calculated blade geometry and to determine if the blade rows experienced negative incidence stall at high through flow conditions.

The mesh constructed using AutoBlade™was sufficient in quality and cell count for this investigation where numerous simulations are needed to obtain a performance map. The mesh did not need any further refinement because the error by increasing the cell count was less than 1% for the design pressure ratio prediction.

The total-to-total pressure ratio prediction of FINE™/Turbo was within 1% for the design point compared to the experimental data of Yan *et al.* (2008). The adiabatic efficiency prediction was considered to be accurate with an error of 4%.

The results predicted the stall region that is defined as a zero gradient region on the pressure performance map. The stall point could not be predicted due to the modelling technique used. The technique used does not simulate the whole blade row and therefore does not model the stall cells between blades.

The compressor did experience negative incidence stall in the stator blade rows at very high mass flow rates according to the off-design correlation of Aungier (2003).

# Chapter 6

# Conclusions and recommendations

The purpose of this chapter is to give an overview of the investigation that was done on the Rofanco 3-stage compressor and the GTHTR300 4-stage helium test compressor. The mathematical model that was used to produce the blade geometries is discussed. A discussion of the results for both compressors is given and some interesting points are mentioned. Finally, recommendations for possible future research are presented.

## 6.1 Mathematical model

The blade geometry for the GTHTR300 4-stage helium test compressor is confidential. Therefore a mathematical model was developed by using the correlations of Lieblein (1960), in conjunction with Dixon (1998) and Aungier (2003). The mathematical model does make some assumptions, for it assumes normal stage loading with the axial velocity remaining constant along the blade span. All the assumptions that were made are justified and within the compressor design guidelines of Aungier (2003). A free vortex design was also implemented to determine the relevant blade angles at at several points along the blade span. Other types of vortex design were investigated, but the free vortex gave sufficient blade profile geometries. The effect of boundary layer blockage at the inlet was also incorporated.

## 6.2 Overview of results

### 6.2.1 Rofanco 3-stage compressor

The blade geometry of the Rofanco 3-stage compressor was reverse engineered as a case study to confirm that the mathematical model produces blade geometries that accurately predict the performance of an axial compressor. The blade geometry obtained from the mathematical model is somewhat different to the exact geometry, however the reaction ratio at mid span is the same

at 0.82. The blade geometry was designed using a free vortex design, and this does not seem to be the case with the exact geometry, due to the large deviations in the camber angle at the hub. The total-to-total pressure ratio prediction obtained from the SUCC do compare adequately with experimental data of Gill (2006)and Roos (1990). The error in the pressure ratio prediction at the design point is less than 1%. This is the norm with this type of code, but it shows that the design that was done by using the mathematical model was sufficient. Thus the mathematical model could be used to determine the blade geometries of the GTHTR300 4-stage helium test compressor with confidence.

## 6.2.2 GTHTR300 4-stage helium test compressor

Proving that the SUCC is a reasonably good code to simulate compressors the GTHTR300 4-stage helium test compressor could be simulated. The SUCC predicted a pressure ratio at the design point within 1% compared to the experimental data of Yan *et al.* (2008). The efficiency that the SUCC predicted was high, but the SUCC did not contain a blade tip clearance loss model. Therefore the blade tip clearance loss model of Aungier (2003) was incorporated to improve the code. After it was incorporated the adiabatic efficiency prediction came to within 2% compared to the experimental data. The SUCC predicted stall in the compressor according to the de Haller stall criterion below 91% design mass flow rate.

An investigation was done to see what effect the boundary layer blockage model as it is incorporated in the SUCC has on the results. The model is based on that of Aungier (2003). It was concluded that this effect had to be considered in the design of blade geometries and therefore it was incorporated into the mathematical model.

By simulating the helium test compressor in 3-dimensions using NUMECA FINE™/Turbo further justified the performance of the calculated blade geometries compared to the experimental data and the SUCC results. The mesh constructed using AutoBlade™ was sufficient in quality and cell count for this investigation where the cell count must be kept to a minimum to shorten computational time and lower the amount of resources required. The mesh did not need any further refinement because the error by increasing the mesh was less than 1% for the design pressure ratio prediction. The $y^+$ values were within acceptable margins for the Spalart-Allmaras turbulence model and the boundary conditions used proved to be adequate and the simulations were stable. The results predicted the stall region that is defined as a zero gradient on the pressure ratio performance map. The SUCC did not predict the stall region, therefore it justifies simulating a compressor in 3-dimensions. The stall point could not be predicted due to the modelling technique used. This technique used does not simulate the whole blade row and therefore does not model the

stall cells between blades. The compressor did experience negative incidence stall in the stator blade row at very high mass flow rates according to the off-design correlation of Aungier (2003).

It can be concluded that the performance of the GTHTR300 4-stage helium test compressor was predicted successfully at high through-flow conditions (roughly 30% more than the design point) with reasonable accuracy and therefore the blade geometries that were reverse engineered are acceptable. There are some deviations between the experimental data at this high mass flow rate, but this is acceptable with the limited knowledge on the helium test compressor.

## 6.3   Recommendations for further work

NUMECA does contain a blade profile optimizer that can be used to obtain a better suited blade profile. The blade profile can be optimized to reduce separation and end wall losses that are particularly relevant on helium compressors as stated in Yan *et al.* (2008).

By using the SUCC, a number of issues were encountered that can be implemented to improve it. Some of these points were also mentioned in Gill (2006) that has still not been resolved. A list of these follows:

- The boundary layer blockage model is unreliable and unstable for the GTHTR300 4-stage helium test compressors and should be improved.

- Improving the loss model so that better correlation is obtained at very high mass flow rates.

- By adding a low Reynolds number model to more accurately predict the stall region.

The compressor can be simulated in the fourth quadrant to identify when negative incidence stall occurs in the rotor blade row and what the performance of the compressor will be. This will entail performing unsteady state simulations to more accurately model the wake that forms behind the blades.

The blade rows as a whole can be simulated with all the blades other than just simulating a blade row passage using FINE™/Turbo. This technique will ensure better correlation in the stall region and will model the stall cells between blades in a blade row more accurately. However this technique requires a large amount of computational resources and time.

# Appendices

# Appendix A

# Blade Profile Geometry

An outline of the mathematical model used to calculate the blade profile geometries is discussed here. The GTHTR300 4-stage helium test compressor is used for illustration. The SUCC uses the ideal gas equations for property calculations, therefore the same equations were used in the mathematical model. The ideal gas constant is taken as 2077.27 J/kg.K for helium at 30°C.

## A.1 Thermodynamic and flow properties

The specific heat is expressed as a polynomial equation that can be seen in equation (A.1.1). (Banerjea $et$ $al.$, 1978)

$$C_p = 5.19 \times 10^3 + 2.28 \times 10^{-2}T - 4.01 \times 10^{-5}T^2 + 3.85 \times 10^{-8}T^3$$
$$-2.06 \times 10^{-11}T^4 + 5.75 \times 10^{-15}T^5 - 6.52 \times 10^{-19}T^6 \quad (A.1.1)$$

The dynamic viscosity is expressed as a Watson distribution and can be seen in equation (A.1.2). (Banerjea $et$ $al.$, 1978)

$$\mu = \frac{\sqrt{T}}{6.7 \times 10^5 - \frac{8 \times 10^7}{T} + \frac{8.27 \times 10^{10}}{T^2} - \frac{1.32 \times 10^{13}}{T^3} + \frac{1.37 \times 10^{15}}{T^4} - \frac{3.2 \times 10^{17}}{T^5}} \quad (A.1.2)$$

The stagnation outlet temperature was then calculated by using the isentropic (adiabatic) efficiency from Dixon (1998) which can be seen in equation (A.1.3).

$$T_{0II} = T_{0I} + \left(\frac{T_{0I}}{\eta_c}\right)\left[\left(\frac{p_{0I}}{p_{0II}}\right)^{\frac{\gamma-1}{\gamma}} - 1\right] \quad (A.1.3)$$

The temperature difference across the compressor was then divided by the number of stages, four, to obtain the temperature rise per stage. The load

coefficient was then calculated by using the enthalpy difference across a stage as in Dixon (1998) and can be seen in (A.1.4).

$$\psi = \frac{h_{02} - h_{01}}{U_{tip}^2} \tag{A.1.4}$$

An iterative process was followed to obtain the static temperature (A.1.5) and pressure (A.1.6) at the inlet for the tip by estimating the inlet absolute velocity. From this, the ideal gas equation was used to calculate the density.

$$T_1 = T_{01} + \frac{C_1^2}{2C_p} \tag{A.1.5}$$

$$p_1 = p_{01} \left( \frac{T_1}{T_{01}} \right)^{\frac{\gamma}{\gamma-1}} \tag{A.1.6}$$

The axial velocity (A.1.7) could then be obtained from the compressor dimensions and so too the flow coefficient (A.1.8) as in Dixon (1998).

$$C_a = \frac{\dot{m}}{\rho_1 A_{inlet}} \tag{A.1.7}$$

$$\phi = \frac{C_a}{U_{tip}} \tag{A.1.8}$$

## A.2   Blade geometry specification

By simultaneously solving the reaction ratio (A.2.1) and load coefficient (A.2.2) equations as in Dixon (1998), the relative flow angles, $\beta_1$ and $\beta_2$, could be calculated by using equation (A.2.3).

$$R = \frac{\phi}{2} \left( \tan\beta_1 + \tan\beta_2 \right) \tag{A.2.1}$$

$$\psi = \phi \left( \tan\beta_1 - \tan\beta_2 \right) \tag{A.2.2}$$

$$\beta = \arctan \left[ \frac{1}{\phi} \left( R + \frac{\psi}{2} \right) \right] \tag{A.2.3}$$

To calculate the absolute flow angles, $\alpha_1$ and $\alpha_2$, equation (A.2.4) can be manipulated to obtain equation (A.2.5).

$$U = C_a \left( \tan\alpha_1 + \tan\beta_1 \right) \tag{A.2.4}$$

$$\alpha = \arctan \left( \frac{1}{\phi} - \tan\beta \right) \tag{A.2.5}$$

Figure 2.2 illustrates the nomenclature used to describe the cascade flow. The angle of attack, $\alpha_{AOA}$ is the angle between the camber line and inlet velocity vector. The stagger or setting angle (A.2.6), $\zeta$, is the angle between

the relative flow angle and angle of attack. The blade angles $\kappa_1$ and $\kappa_2$ are the angles between the axial direction and the camberline at the leading and trailing edges, respectively. The blade camber angle (A.2.7) is defined as the difference between the blade angles, $\kappa_1$ and $\kappa_2$. (Aungier, 2003)

$$\zeta = \beta_1 - \alpha_{AOA} \tag{A.2.6}$$

$$\theta = \kappa_1 - \kappa_2 \tag{A.2.7}$$

By using the flow angles, an estimate of the camber angle ($\theta_{est}$) can be obtained for the rotor by using (A.2.8). For the stator, the relative flow angles, $\beta$, are replaced by the corresponding absolute flow angles, $\alpha$.

$$\theta_{est} = \beta_1 - \beta_2 \tag{A.2.8}$$

The camber and stagger angles is obtained by using the design angle of attack (A.2.9), design incidence (A.2.10) and design deviation (A.2.11) angles as in Aungier (2003). The $t_b/c$ was taken as 0.1 and NACA 65-series blades were chosen. For NACA 65-series blades with $t_b/c = 0.1$ the $K_{sh} = K_{t,i} = K_{t,\delta} = 1$ and $(a/c) = 0.5$.

$$\alpha^* = \left[ 3.6 K_{sh} K_{t,i} + 0.3532 \theta \left( a/c \right)^{0.25} \right] \sigma^{0.65 - 0.002\theta} \tag{A.2.9}$$

$$i^* = K_{sh} K_{t,i} \left( i_0^* \right)_{10} + n\theta \tag{A.2.10}$$

where

$$i_0^* = \frac{\beta_1^{\left( 0.914 + \sigma^3/160 \right)}}{5 + 46 \exp\left( -2.3\sigma \right)} - 0.1\sigma^3 \exp\left[ \left( \beta_1 - 70 \right)/4 \right]$$

and

$$n = 0.025\sigma - 0.06 - \frac{\left( \beta_1/90 \right)^{\left( 1 + 1.2\sigma \right)}}{1.5 + 0.43\sigma}$$

with $\beta_1$ in degrees.

$$\delta^* = K_{sh} K_{t,\delta} \left( \delta_0^* \right)_{10} + m\theta \tag{A.2.11}$$

where

$$\delta_0^* = 0.01\sigma\beta_1 + \left[ 0.74\sigma^{1.9} + 3\sigma \right] \left( \beta_1/90 \right)^{\left( 1.67 + 1.09\sigma \right)}$$

and

$$m = \frac{0.17 - 0.0333 \left( \beta_1/100 \right) + 0.333 \left( \beta_1/100 \right)^2}{\sigma^{0.9625 - 0.17(\beta_1/100) - 0.85(\beta_1/100)^3}}$$

with $\beta_1$ in degrees.

As can be seen in equation (A.2.10) and (A.2.11) the camber angle is needed. An estimate of the camber angle was used as can be seen in equation (A.2.8). The calculations were iterated so that the difference between consecutive camber angles was $1 \times 10^{-6}$.

By using equation (A.2.12) and equation (A.2.13) the camber and stagger angles can be calculated as shown in equation (A.2.7) and (A.2.6), respectively.

$$\kappa_1 = \beta_1 - i^* \tag{A.2.12}$$

$$\kappa_2 = \beta_2 - \delta^* \tag{A.2.13}$$

## A.3   Free vortex design and casing geometry

To calculate the camber and stagger angles at different points on the blade span, a free vortex design (A.3.1) can be implemented as in Dixon (1998).

$$C_x r = const \tag{A.3.1}$$

It is assumed that $C_a$ is constant throughout the compressor, therefore equation (A.3.1) can be simplified as follows. The subscript (*des*) and (*ref*) donates the desired and reference point, respectively.

$$
\begin{aligned}
C_{a,des} \tan \alpha_{des} r_{des} &= C_{a,ref} \tan \alpha_{ref} r_{ref} \\
\tan \alpha_{des} r_{des} &= \tan \alpha_{ref} r_{ref} \\
\tan \alpha_{des} &= (r_{ref}/r_{des}) \tan \alpha_{ref} \\
\alpha_{des} &= \arctan\left[(r_{ref}/r_{des}) \tan \alpha_{ref}\right]
\end{aligned}
\tag{A.3.2}
$$

Equation (A.3.2) is used to calculate the angle at the desired point. The same equation can be used to calculate the angle at any other point on the blade span by changing the desired point if the reference point is known.

The same procedure as stated above between equation (A.2.9) and (A.2.13) is followed to calculate the camber and stagger angles at the desired point on the blade span.

The same method was used to calculate the angles for the stator blades. Normal stage loading was assumed and so too a constant hub diameter. The casing was tapered by using the method described below. The blade tip clearance is 1% of the blade span. The casing was modelled with a straight line. The exit blade height was then used to calculate the gradient.

$$A_{exit} = \frac{A_{inlet}}{\rho_{ratio}}$$

$$D_{exit,casing} = \sqrt{\frac{4A_{exit}}{\pi} + D_{hub}^2}$$

$$h_{exit} = 0.99 \frac{D_{exit,casing} - D_{hub}}{2}$$

# Appendix B

# Off-design cascade performance

The SUCC utilizes the off-design cascade performance correlation of Aungier (2003). This model is used to compute the loss coefficient from the positive and negative stall incidence angles by including the Mach number effect.

## B.1 Positive and negative stall incidence angles

It starts off by calculating the negative and positive stall incidence angles by iteration of equations (B.1.1) and (B.1.2), respectively, as $\alpha$ is a function of $\beta_1$. All angles are expressed in degrees where a lower limit $\beta_{1c} \geq 20°$ is applied as proposed by (Aungier, 2003).

$$\alpha_c - \alpha^* = -9 + \left[ 1 - \left( \frac{30}{\beta_{1c}} \right)^{0.48} \right] \frac{\theta}{4.176} \tag{B.1.1}$$

$$\alpha_s - \alpha^* = 10.3 + \left[ 2.92 - \frac{\beta_{1s}}{15.6} \right] \frac{\theta}{8.2} \tag{B.1.2}$$

This correlation is based upon the work of Emery *et al.* (1957) and was developed from NACA 65-series low Mach number two-dimensional cascade test data. Since $\alpha - \alpha^*$ is simply the incidence angle range to stall, these correlations can also be used for other types of profiles besides NACA 65-series profiles (Aungier, 2003).

## B.2 Mach number effects

Figure B.1 is a schematic showing the variation of loss coefficient with incidence and is referred to as the loss bucket. The negative and positive loss ranges for low-speed cascades are termed $R_c$ and $R_s$, equations (B.2.1) and (B.2.2), respectively. As the Mach number increases, the loss bucket ranges are reduced roughly by the same amount (Aungier, 2003). For high Mach numbers $R_c$ reduces faster than $R_s$.
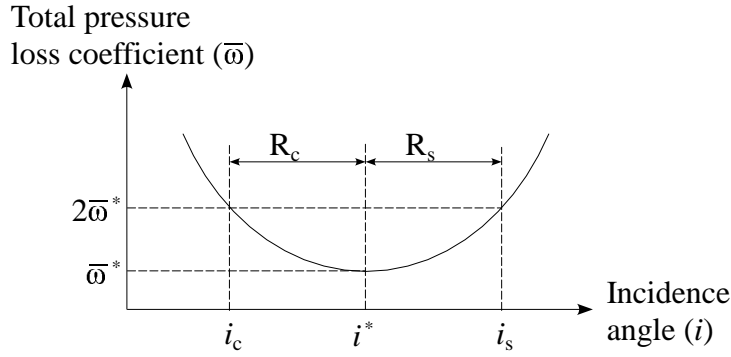
Figure B.1: Schematic showing the variation of loss coefficient with incidence

$$R_c = \alpha^* - \alpha_c = i^* - i_c \qquad (B.2.1)$$

$$R_s = \alpha_s - \alpha^* = i_s - i^* \qquad (B.2.2)$$

The negative, $i_c$, and positive, $i_s$, stall incidence angles are calculated from equations (B.2.3) and (B.2.4), but with the constraint that $(K_i)_{sh} \leq 1$.

$$i_c = i^* - \frac{R_c}{1 + 0.5 M_1'^3} \qquad (B.2.3)$$

$$i_s = i^* + \frac{R_s}{1 + 0.5 \left[ (K_i)_{sh} M_1' \right]^3} \qquad (B.2.4)$$

The minimum loss incidence angle, $i_m$, is calculated from equations (B.2.5) for elevated Mach numbers.

$$i_m = i_c + \frac{(i_s - i_c) R_c}{R_c + R_s} \qquad (B.2.5)$$

To obtain the design incidence pressure loss coefficient, the equivalent diffusion factor, $D_{eq}^*$, based upon blades operating at minimum loss is needed. Lieblein (1959) developed a correlation for this equivalent diffusion factor at design incidence angle and can be seen in equation (B.2.6), as stated by Aungier (2003).

$$D_{eq}^* = \frac{\cos \beta_2^*}{\cos \beta_1^*} \left[ 1.12 + 0.61 \frac{\cos^2 \beta_1^*}{\sigma} \left( \tan \beta_1^* - \tan \beta_2^* \right) \right] \qquad (B.2.6)$$

The design incidence pressure loss coefficient, $\bar{\omega}^*$, can be calculated from equation (B.2.7).

$$\bar{\omega}^* = \frac{2\sigma K_1}{\cos \beta_2^*} \left( \frac{\cos \beta_1^*}{\cos \beta_2^*} \right)^2 \left[ K_2 + 3.1 \left( D_{eq}^* - 1 \right)^2 + 0.4 \left( D_{eq}^* - 1 \right)^8 \right] \qquad (B.2.7)$$

where

$$K_1 = 0.004$$

and

$$K_2 = 1 + \frac{s}{h} \cos \beta_2^* + 0.004 \frac{K_{Re}}{K_1}$$

The correction parameters $K_1$, $K_2$ and $K_{Re}$ were obtained by Aungier (2003). The first two parameters, $K_1$ and $K_2$ are included to adjust the profile loss model to compensate for other loss sources, such as end-wall and secondary flow losses. These parameters were obtained by comparing the performance prediction to experimental data for various axial flow compressors. The last parameter, $K_{Re}$, is based upon the blade chord Reynolds number and was derived from Reynolds number formulations for boundary layer skin friction coefficients. The skin friction models used can be found in Schlichting (1968, 1979). For laminar flow refer to equation (B.2.8) and for turbulent flow refer to equation (B.2.9).

$$K_{Re} = \sqrt{\frac{2.5 \times 10^5}{Re_c} - 1}; Re < 2.5 \times 10^5 \tag{B.2.8}$$

$$K_{Re} = \left[ \frac{\log (2.5 \times 10^5)}{\log Re_c} \right]^{2.58} - 1; Re > 2.5 \times 10^5 \tag{B.2.9}$$

## B.3   Off-design correlation

A normalized incidence angle parameter, $\xi$, is defined in equations (B.3.1) and (B.3.2), and used to calculate the off-design loss coefficient.

$$\xi = \frac{i - i_m}{i_m - i_s}; i \geq i_m \tag{B.3.1}$$

$$\xi = \frac{i - i_m}{i_m - i_s}; i < i_m \tag{B.3.2}$$

The minimum loss coefficient, $\bar{\omega}_m$, can be calculated from equation (B.3.3). For incidence angles between $i_c$ and $i_s$, Aungier (2003) propose the use of a second order power law relation for the off-design loss coefficient.

$$\bar{\omega}_m = \bar{\omega}^* \left[ 1 + \left( \frac{i_m - i^*}{R_s} \right)^2 \right] \tag{B.3.3}$$

The loss coefficient is calculated from equation (B.3.4) that is a parabolic loss bucket with equations (B.3.5) and (B.3.6) being linear extrapolations outside the range. Figure 2.4 shows the loss bucket with the linear extrapolations.

$$\bar{\omega} = \bar{\omega}_m \left[ 1 + \xi^2 \right] ; -2 \leq \xi \leq 1 \tag{B.3.4}$$

$$\bar{\omega} = -\bar{\omega}_m \left[ 3 + 4\xi \right] ; \xi < -2 \tag{B.3.5}$$

$$\bar{\omega} = \bar{\omega}_m \left[ 2\xi \right] ; \xi > 1 \tag{B.3.6}$$

# Appendix C

# Sample calculation for negative incidence stall correlation

This chapter contains a sample calculation to identify if negative incidence stall has occurred in a blade row. The theory used in this chapter is covered in Appendix B. The data represent that of the GTHTR300 4-stage helium test compressor at mid span under abnormal conditions. The mass flow rate trough the compressor is much higher at 16 kg/s, roughly 130% of the design mass flow rate. The total-to-total pressure ratio at this point is 1.003, thus there is almost no pressure rise across it. The sample calculation is done for the last rotor blade row of the compressor, as the first rotor blade row is closer to the design incidence angle.

The blade angles $\kappa_1$ and $\kappa_1$ are obtained from Appendix A and are shown below. From this, the blade camber angle, $\theta$, equation (A.2.7) is known.

$$\kappa_1 = 61.4° \; ; \; \kappa_2 = 45.4°$$
$$\theta = \kappa_1 - \kappa_2 = 16°$$

The relative flow angles and velocities for the inlet and outlet of the last rotor blade row were extracted from NUMECA CFView™ version 8, and is shown below. CFView™ is the flow visualization and post-treatment package of NUMECA.

$$\beta_1 = 56.2° \; ; \; W_1 = 354.819 \; m/s$$
$$\beta_2 = 51.2° \; ; \; W_2 = 351.284 \; m/s$$

By using this the design angle of attack, $\alpha^*$, equation (A.2.9), design incidence, $i^*$, equation (A.2.10) and design deviation, $\delta^*$, equation (A.2.11) angles can be calculated.

$$\alpha^* = 8.9° \; ; \; i^* = 1.6° \; ; \; \delta^* = 5.5°$$

From this, the relative design angles, $\beta_1^*$ and $\beta_2^*$ can be calculated.

$$\beta_1^* = i^* + \kappa_1 = 63°$$
$$\beta_2^* = \delta^* + \kappa_2 = 50.9°$$

The negative, $R_c$, and positive, $R_s$, loss ranges can be calculated from equations (B.2.1) and (B.2.2), respectively.

$$R_c = 8° \; ; \; R_s = 9°$$

The negative, $i_c$, positive , $i_s$, and mean , $i_m$, stall incidence angles can be calculated from equations (B.2.3), (B.2.4) and (B.2.5), respectively.

$$i_c = -6.2° \; ; \; i_s = 10.4° \; ; \; i_m = 9.5°$$

The equivalent diffusion factor, $D_{eq}^*$, based upon blades operating at minimum loss is obtained from equation (B.2.6).

$$D_{eq}^* = 0.817$$

The design incidence pressure loss coefficient, $\bar{\omega}^*$, is calculated from equation (B.2.7).

$$\bar{\omega}^* = 0.017$$

To determine what the incidence angle, $i$, is the results from CFView™ were used.

$$i = \beta_1 - \kappa_1 = -5.118°$$

As the incidence angle is less than the mean stall incidence angle, $i < i_m$, the normalized incidence angle parameter, $\xi$, is calculated using equations (B.3.2).

$$\xi = -0.93$$

The minimum loss coefficient, $\bar{\omega}_m$, is obtained using equations (B.3.3).

$$\bar{\omega}_m = 0.029$$

According to the correlation of Aungier (2003), the minimum loss coefficient is still within the parabolic region of the loss bucket, refer to Appendix B and figure 2.4. Therefore the loss coefficient, $\bar{\omega}$, is calculated using equation (B.3.4).

$$\bar{\omega} = 0.053 < 2\bar{\omega}_m$$

As the loss coefficient is less than twice the minimum loss coefficient, it shows that the last rotor blade row is not experiencing negative incidence stall.

# Appendix D

# Sample input for the SUCC

This chapter contains the input file content of the SUCC for the GTHTR300 4-stage helium test compressor. Details on interpreting the input file can be found in Thiart (2004).

`GTHTR300.def`

```
! GTHTR300 4-stage helium test compressor
! - Deviation and primary loss model: Aungier
! - Secondary loss model: None
! - Boundary layers: default (Aungier)

! Compressor definition: annulus
! - hubr hubz  casr  casz  Nhub  Ncas
! Inlet
S1 0.25 0 0.284 0 10962 0
! ROTOR 1
S2 0.25 0.13 0.284 0.131 10962 0
S3 0.25 0.146 0.283895738 0.145 10962 0
! STATOR 1
S4 0.25 0.164 0.283754238 0.164 10962 0
S5 0.25 0.1825 0.283616463 0.1825 10962 0
! ROTOR 2
S6 0.25 0.1995 0.283482411 0.2005 10962 0
S7 0.25 0.2155 0.283378148 0.2145 10962 0
! STATOR 2
S8 0.25 0.2335 0.283236649 0.2335 10962 0
S9 0.25 0.252 0.283098873 0.252 10962 0
! ROTOR 3
S10 0.25 0.269 0.282964821 0.27 10962 0
S11 0.25 0.285 0.282860558 0.284 10962 0
! STATOR 3
```

```
S12 0.25 0.303 0.282719059 0.303 10962 0
S13 0.25 0.3215 0.282581283 0.3215 10962 0
! ROTOR 4
S14 0.25 0.3385 0.282447231 0.3395 10962 0
S15 0.25 0.3545 0.282342968 0.3535 10962 0
! STATOR 4
S16 0.25 0.3725 0.282201469 0.3725 10962 0
S17 0.25 0.391 0.282063693 0.391 10962 0
! Exit
S18 0.25 0.406 0.282063693 0.406 10962 0
S19 0.25 0.52 0.282063693 0.52 10962 0


! Compressor definition: bleeds (no bleeds)

! Compressor definition: bladerows
 BLADEROWS
 ROTOR 1 10962 72 AUNGIER AUNGIER CONSTANT 0 LE S2 NACA65 TABLE
 FILE C:\Werk\Tesis\SUCC\Applications\GTHTR300_4Stages\r1.txt
 STATOR 1 94 MIRROR AUNGIER AUNGIER CONSTANT 0 LE S4 NACA65 TABLE
 FILE C:\Werk\Tesis\SUCC\Applications\GTHTR300_4Stages\s1.txt
 ROTOR 2 10962 72 AUNGIER AUNGIER CONSTANT 0 LE S6 NACA65 TABLE
 FILE C:\Werk\Tesis\SUCC\Applications\GTHTR300_4Stages\r2.txt
 STATOR 2 94 MIRROR AUNGIER AUNGIER CONSTANT 0 LE S8 NACA65 TABLE
 FILE C:\Werk\Tesis\SUCC\Applications\GTHTR300_4Stages\s2.txt
 ROTOR 3 10962 72 AUNGIER AUNGIER CONSTANT 0 LE S10 NACA65 TABLE
 FILE C:\Werk\Tesis\SUCC\Applications\GTHTR300_4Stages\r3.txt
 STATOR 3 94 MIRROR AUNGIER AUNGIER CONSTANT 0 LE S12 NACA65 TABLE
 FILE C:\Werk\Tesis\SUCC\Applications\GTHTR300_4Stages\s3.txt
 ROTOR 4 10962 72 AUNGIER AUNGIER CONSTANT 0 LE S14 NACA65 TABLE
 FILE C:\Werk\Tesis\SUCC\Applications\GTHTR300_4Stages\r4.txt
 STATOR 4 94 MIRROR AUNGIER AUNGIER CONSTANT 0 LE S16 NACA65 TABLE
 FILE C:\Werk\Tesis\SUCC\Applications\GTHTR300_4Stages\s4.txt

! Operating conditions: stagnation pressure & temperature, and mass flow
 CONSTANT 896000 300.05 12.3

! Operating conditions: boundary layer thickness (optional)
 BLB 0.01 0.01

! Thermodynamic properties
 IDEALGAS 2077.27
 POLYNOMIAL 5.18879e3 2.27544e-2 -4.00688e-5 3.85245e-8 -2.06087e-11
 5.74987e-15 -6.51527e-19
 WATSON 6.70E+05 -8.00E+07 8.27E+10 -1.32E+13 1.37E+15 -3.20E+17
```

```
! Computational grid: quasi-streamlines
 CONSTANT 3
 CONSTANT S1 5
 CONSTANT S18 5

! Computational method
 MTFM FD MSI 0.1 DEFAULT 0.08

! Compressor map
 SPEED
! ---- N% m% +m% delm%
 LINE 101.2 70 130 1

! Initial conditions
 STRATEGIC

----------------------------------------------------------------
r1.txt

0.000 0.026 50.746 0.000 Rotor101 18.949 0.100
0.125 0.026 51.554 0.000 Rotor102 18.134 0.100
0.250 0.026 52.327 0.000 Rotor103 17.369 0.100
0.375 0.026 53.066 0.000 Rotor104 16.649 0.100
0.500 0.026 53.773 0.000 Rotor105 15.973 0.100
0.625 0.026 54.451 0.000 Rotor106 15.336 0.100
0.750 0.026 55.101 0.000 Rotor107 14.736 0.100
0.875 0.026 55.725 0.000 Rotor108 14.170 0.100
1.000 0.026 56.325 0.000 Rotor109 13.635 0.100
----------------------------------------------------------------
s1.txt

0.000 0.020 20.129 0.000 Stator101 42.670 0.100
0.125 0.020 19.937 0.000 Stator102 42.340 0.100
0.250 0.020 19.748 0.000 Stator103 42.015 0.100
0.375 0.020 19.560 0.000 Stator104 41.694 0.100
0.500 0.020 19.375 0.000 Stator105 41.378 0.100
0.625 0.020 19.192 0.000 Stator106 41.066 0.100
0.750 0.020 19.012 0.000 Stator107 40.758 0.100
0.875 0.020 18.834 0.000 Stator108 40.455 0.100
1.000 0.020 18.658 0.000 Stator109 40.157 0.100
----------------------------------------------------------------
r2.txt
```

```
0.000 0.026 50.746 0.000 Rotor201 18.949 0.100
0.125 0.026 51.554 0.000 Rotor202 18.134 0.100
0.250 0.026 52.327 0.000 Rotor203 17.369 0.100
0.375 0.026 53.066 0.000 Rotor204 16.649 0.100
0.500 0.026 53.773 0.000 Rotor205 15.973 0.100
0.625 0.026 54.451 0.000 Rotor206 15.336 0.100
0.750 0.026 55.101 0.000 Rotor207 14.736 0.100
0.875 0.026 55.725 0.000 Rotor208 14.170 0.100
1.000 0.026 56.325 0.000 Rotor209 13.635 0.100
-------------------------------------------------------------
s2.txt

0.000 0.020 20.129 0.000 Stator201 42.670 0.100
0.125 0.020 19.937 0.000 Stator202 42.340 0.100
0.250 0.020 19.748 0.000 Stator203 42.015 0.100
0.375 0.020 19.560 0.000 Stator204 41.694 0.100
0.500 0.020 19.375 0.000 Stator205 41.378 0.100
0.625 0.020 19.192 0.000 Stator206 41.066 0.100
0.750 0.020 19.012 0.000 Stator207 40.758 0.100
0.875 0.020 18.834 0.000 Stator208 40.455 0.100
1.000 0.020 18.658 0.000 Stator209 40.157 0.100
-------------------------------------------------------------
r3.txt

0.000 0.026 50.746 0.000 Rotor301 18.949 0.100
0.125 0.026 51.554 0.000 Rotor302 18.134 0.100
0.250 0.026 52.327 0.000 Rotor303 17.369 0.100
0.375 0.026 53.066 0.000 Rotor304 16.649 0.100
0.500 0.026 53.773 0.000 Rotor305 15.973 0.100
0.625 0.026 54.451 0.000 Rotor306 15.336 0.100
0.750 0.026 55.101 0.000 Rotor307 14.736 0.100
0.875 0.026 55.725 0.000 Rotor308 14.170 0.100
1.000 0.026 56.325 0.000 Rotor309 13.635 0.100
-------------------------------------------------------------
s3.txt

0.000 0.020 20.129 0.000 Stator301 42.670 0.100
0.125 0.020 19.937 0.000 Stator302 42.340 0.100
0.250 0.020 19.748 0.000 Stator303 42.015 0.100
0.375 0.020 19.560 0.000 Stator304 41.694 0.100
0.500 0.020 19.375 0.000 Stator305 41.378 0.100
0.625 0.020 19.192 0.000 Stator306 41.066 0.100
0.750 0.020 19.012 0.000 Stator307 40.758 0.100
0.875 0.020 18.834 0.000 Stator308 40.455 0.100
```

```
1.000  0.020  18.658  0.000  Stator309  40.157  0.100a
----------------------------------------------------------------
r4.txt

0.000  0.026  50.746  0.000  Rotor401  18.949  0.100
0.125  0.026  51.554  0.000  Rotor402  18.134  0.100
0.250  0.026  52.327  0.000  Rotor403  17.369  0.100
0.375  0.026  53.066  0.000  Rotor404  16.649  0.100
0.500  0.026  53.773  0.000  Rotor405  15.973  0.100
0.625  0.026  54.451  0.000  Rotor406  15.336  0.100
0.750  0.026  55.101  0.000  Rotor407  14.736  0.100
0.875  0.026  55.725  0.000  Rotor408  14.170  0.100
1.000  0.026  56.325  0.000  Rotor409  13.635  0.100
----------------------------------------------------------------
s4.txt

0.000  0.020  20.129  0.000  Stator401  42.670  0.100
0.125  0.020  19.937  0.000  Stator402  42.340  0.100
0.250  0.020  19.748  0.000  Stator403  42.015  0.100
0.375  0.020  19.560  0.000  Stator404  41.694  0.100
0.500  0.020  19.375  0.000  Stator405  41.378  0.100
0.625  0.020  19.192  0.000  Stator406  41.066  0.100
0.750  0.020  19.012  0.000  Stator407  40.758  0.100
0.875  0.020  18.834  0.000  Stator408  40.455  0.100
1.000  0.020  18.658  0.000  Stator409  40.157  0.100
----------------------------------------------------------------
```

# List of References

Aungier, R. (2000). *Centrifugal compressors: a strategy for aerodynamic design and analysis.* ASME Press, New York, NY.

Aungier, R. (2003). *Axial-flow compressors: A strategy for aerodynamic design and analysis.* ASME Press, New York, NY.

Banerjea, A., Hammeke, K., Hüpping, Kipke, H. and Stoehr (1978). *Thermo-dynamische Stoffwerte von Helium im Bereich von 20 bis 1 500 ˚C und 1 bis 100 bar.* Kernforschungsanlage Jülich GmbH. (Kerntechnischen Ausschusses Daten).

Benade, T. (1987). Die herontwerp van die Rofanco kompressor. Internal Report, Faculty of Engineering, University of Stellenbosch.

Cumpsty, N. (1989). *Compressor aerodynamics.* Longman Scientific and Technical.

Dixon, S. (1998). *Fluid mechanics, thermodynamics of turbomachinery.* Butterworth-Heinemann, Boston.

Emery, J., Herrig, L., Erwin, J. and Felix, A. (1957). Systematic two-dimensional cascade tests of NACA 65-series compressor blades at low speeds. *NACA TN 3916.*

Fujikawa, S., Hayashi, H., Nakazawa, T., Kawasaki, K., Iyoku, T., Nakagawa, S. and Sakaba, N. (2004). Achievement of reactor-outlet coolant temperature of 950° C in HTTR. *Journal of Nuclear Science and Technology*, vol. 41, no. 12, pp. 1245–1254.

Gill, A. (2006). *A comparison between stall prediction models for axial flow compressors.* Master's thesis, University of Stellenbosch, Faculty of Engineering.

Gill, A. (2007). Fundamentals of four-quadrant axial flow compressor maps. *Proc. IMechE, Journal Power and Energy*, vol. 221.

Gill, A. (2009). The Stellenbosch University Compressor Code (SUCC) and NUMECA. Private communication and aid.

Gill, A., von Backström, T. and Harms, T. (2009). The flow field within an axial flow compressor at extremely high flow coefficients. *ASME, Journal of Turbomachinery.*

Grüber, B. and Carstens, V. (2001). The impact of viscous effects on the aerodynamic damping of vibrating transonic compressor blades - a numerical study. *ASME, Journal of Turbomachinery*, vol. 123, pp. 409–417.

Horlock, J. and Denton, J. (2005). A review of some early design practice using computational fluid dynamics and a current perspective. *ASME, Journal of Turbomachinery*, vol. 127, pp. 5–13.

Howell, A. (1945). Design of axial compressors. *Proceedings of the Institution of Mechanical Engineers*, vol. 153, London, United Kingdom.

Johnsen, I. and Bullock, R. (1965). Aerodynamic design of axial flow compressors. NASA SP-36, NASA, Washington DC.

Lewis, K. (1989). *Prediction of stall inception in an axial flow compressor.* Master's thesis, University of Stellenbosch, Faculty of Engineering.

Lieblein, S. (1959). Loss and stall analysis of compressor cascades. *ASME, Journal of Basic Engineering*, vol. 81, pp. 387–400.

Lieblein, S. (1960). Incidence and deviation-angle correlations for compressor cascades. *ASME, Journal of Basic Engineering*, pp. 575–587.

Lieblein, S., Broderick, R. and Schwenk, F. (1953). *Diffusion factor for estamating losses and limiting blade loadings in axial-flow-compressor blade elements.* NACA, Washington, DC.

Pampreen, R. (1993). *Compressor surge and stall.* Concepts ETI.

Pratap, A., M.S. and Geetha, P. (2005). Improvement of a multi-stage transonic compressor using cfd. *ISABE Procedings, ISABE 2005-1267.*

Roos, T. (1990). Reblading and testing of the Rofanco low speed axial flow compressor. Undergraduate final year project, Faculty of Engineering, University of Stellenbosch.

Roos, T. (1995). *A prediction method for flow in axial flow compressors.* Master's thesis, University of Stellenbosch, Faculty of Engineering.

Schlichting, H. (1968). *Boundary-layer theory.* McGraw-Hill, New York.

Schlichting, H. (1979). *Boundary-layer theory.* McGraw-Hill, New York.

Takizuka, T., Takada, S., Yan, X., Kosugiyama, S., Katanishi, S. and Kunitomi, K. (2004). R&D on the power conversion system for gas turbine high temperature reactors. *Nuclear Engineering and Design*, vol. 233, no. 1-3, pp. 329–346.

Thiart, G. (2004). The Stellenbosch University Compressor Code (SUCC), Faculty of Engineering, University of Stellenbosch.

Weisbrodt, I. (1995). Summary report of technical experiences from high-temperature helium turbo-machinery testing in Germany. Tech. Rep., IAEA-TECDOC-899, pp. 177 to 248, International Atomic Energy Agency, Vienna, Austria.

Yan, X., Takizuka, T., Kunitomi, K., Itaka, H. and Takahashi, K. (2008). Aerodynamic Design, Model Test, and CFD Analysis for a Multistage Axial Helium Compressor. *Journal of Turbomachinery*, vol. 130, p. 031018.

Yan, X., Takizuka, T., Takada, S., Kunitomi, K., Minatsuki, I. and Mizokami, Y. (2003). Cost and performance design approach for GTHTR300 power conversion system. *Nuclear Engineering and Design*, vol. 226, no. 3, pp. 351–373.